Contact Mistuning Identification in Bladed Disks Using Limited Experimental Data and Data-Driven Techniques

applied sciences

Article

Contact Mistuning Identification in Bladed Disks Using Limited Experimental Data and Data-Driven Techniques

Umidjon Usmanov *, Christian Maria Firrone and Giuseppe Battiato

Department of Mechanical and Aerospace Engineering, Politecnico di Torino, Corso Duca Degli Abruzzi 24, 10129 Turin, Italy
* Correspondence: umidjon.usmanov@polito.it

Abstract

Contact-induced mistuning at the blade–disk interface is a major source of variability in the dynamic response of bladed disks, yet its identification remains challenging due to the intrinsic complexity of the contact phenomenon. Contact mistuning in this framework is defined as the variation of the contact topology at the blade–disk interface, i.e., the spatial distribution of contacting and non-contacting regions governing the mechanical interaction between components. This work proposes a data-driven framework for the identification of contact mistuning based on a reduced set of experimentally measured maps. A statistical representation of the contact space is constructed using Principal Component Analysis. This representation is subsequently exploited to generate physically consistent synthetic contact patterns. These are combined with blade intrinsic mistuning parameters to build a dataset linking contact conditions and blade variability to the natural frequencies of a disk–one-blade assembly. A k-nearest neighbors algorithm is employed for inverse identification using a subset of measured natural frequencies. The identification relies on modes selected through sensitivity analysis, and robustness is improved using a weighted distance metrics. The methodology is validated using both a reduced-order model based digital twin and experimental data. The results show accurate identification of contact patterns, confirmed through comparison of modal properties of the full mistuned assembly. Therefore, the proposed framework provides a practical tool for the experimental identification of contact mistuning in bladed disks.

Keywords: bladed disks; contact mistuning; reduced-order modeling; principal component analysis; inverse identification

1. Introduction

Bladed disks are highly sensitive to small structural variations between individual blades. In practice, perfectly periodic assemblies do not exist, as unavoidable deviations introduced during manufacturing, assembly, or operation lead to blade-to-blade variability [1]. Although these deviations are often small, their influence on the behavior of the assembly can be substantial, producing large amplification of the dynamic response with respect to those expected in an ideal tuned configuration [2,3]. As a consequence, certain blades may experience vibration levels significantly higher than those predicted for a tuned system, increasing the susceptibility to high-cycle fatigue damage.

From a computational perspective, the analysis of mistuned bladed disks represents a challenging problem. Accurate prediction of the dynamic behavior generally requires high-fidelity finite element models (FEM) capable of representing blade-to-blade variability

Academic Editor: Rui Araújo

Received: 30 June 2026
Revised: 25 July 2026
Accepted: 31 July 2026
Published: 1 August 2026

across the entire assembly. The resulting numerical models often involve extremely large numbers of degrees of freedom (DOF), making numerical analyses computationally demanding, especially in probabilistic or Monte-Carlo simulations. Moreover, the relationship between mistuning parameters and the global dynamic response is highly nontrivial, which further complicates the modeling of mistuned systems.

To overcome these limitations, reduced-order models (ROMs) can be derived from finite element representations of the structure. In this framework, the essential dynamic characteristics of the structure are retained while significantly reducing the number of DOFs of the system. This enables accurate prediction of the dynamic response while maintaining computational efficiency. Several ROM strategies have been proposed for the analysis of small mistuning in bladed disks. Among them, system-level approaches represent the dynamics of the mistuned assembly through combinations of tuned-system modes, whereas component-level techniques perform the reduction separately on the individual substructures, such as blades and disk sectors [4–6]. Other methodologies formulate mistuning as a perturbation of the nominal tuned configuration and derive the mistuned response through correction operators applied to the baseline dynamic model [7,8]. System-level reduced-order approaches were first introduced by Yang and Griffin [5], who represented the mistuned response as a combination of tuned-system modes. This concept was later extended through the Fundamental Model of Mistuning (FMM) proposed by Feiner and Griffin [9], which formulates the problem at the level of a single modal family using only the nominal frequencies and blade mistuning parameters. Component-level approaches perform model reduction at the level of individual substructures, typically separating blades and disk. Early contributions by Castainer et al. [6] introduced formulations based on sector-level component modes, where mistuning is incorporated directly through blade properties. The work of Bladh et al. [10,11] introduced mistuning modeling framework called Component Mode Mistuning (CMM), which employs the Craig–Bampton method and secondary reduction strategies, achieving significant reductions in model size. Later contributions generalized the framework to account for both stiffness and mass mistuning [12], and proposed modular formulations enabling independent treatment of blade and disk variations [13]. Following the development of ROMs for small stiffness mistuning, subsequent studies extended these methodologies to account for additional sources of variability, including geometric mistuning [14–16], large mistuning [17], and damping mistuning [18,19]. ROM formulations accounting for the nonlinear behavior of frictional joint interfaces have also been proposed in the literature [20–22].

In addition to the conventional blade-to-blade variability, mistuning may also originate from variations in the contact conditions at the blade–disk interface. Petrov and Ewins [23] highlighted that scatter in contact interface characteristics, such as shroud gaps, friction dampers, and blade–root contacts, can significantly influence the nonlinear forced response of bladed disks. Avalos et al. [24] further investigated the effects of blade–disk interface variability by introducing stochastic variations in the interface properties, showing that interface mistuning may produce response amplification levels even higher than those associated with conventional blade frequency mistuning. More recently, Krizak et al. [25] proposed a ROM framework capable of simultaneously accounting for stiffness mistuning and contact variability at the blade root joint. Pinto et al. [26] proposed a ROM framework for incorporating contact mistuning at the blade–root interface based on Craig–Bampton and Gram–Schmidt Interface reductions [27]. The methodology introduced both measurement-based and generic strategies for constructing the interface reduction basis, while subsequent experimental investigations validated the approach through pressure-film contact measurements [28]. Recently, the authors proposed two complementary data-driven frameworks for blade–disk contact mistuning. The first addressed the statistical reconstruction of contact patterns from a limited number of experimentally measured pressure-film imprints [29], while the second introduced an approach to identify unknown contact patterns from modal characteristics [30]. However, both studies were limited to numerical investigations, did not account for blade mistuning, and did not include experimental validation through testing of the actual components.

Despite these developments, existing studies have mainly focused on modeling the influence of interface variability on the dynamic response or on incorporating measured contact conditions into ROMs. However, despite the significant research effort devoted to contact mistuning, the identification of contact conditions at the blade–disk interface remains an open problem.

The present work addresses this gap by proposing a data-driven framework for the identification of contact mistuning in bladed disks using limited experimental information. A ROM of the assembly is constructed by combining Craig–Bampton reduction for the disk and Rubin free-interface reduction for the blade. Within this framework, blade mistuning is introduced through perturbations of the free-interface natural frequencies, while contact mistuning is represented through variations of the contact topology at the blade–disk interface. Starting from a reduced set of experimentally measured pressure-film imprints, a statistical representation of the contact space is constructed using Principal Component Analysis (PCA). This representation is then exploited to generate synthetic yet physically consistent contact patterns spanning the admissible contact variability. The generated patterns are combined with blade mistuning parameters and introduced into a disk–one-blade ROM to construct a dataset linking contact conditions to the corresponding natural frequencies of the assembly. Finally, the identification of unknown contact patterns is performed through a k-nearest neighbors (k-NN) algorithm based on experimentally measured modal data. The proposed methodology is validated through comparison with experimental results obtained on both disk–one-blade and full-bladed disk assemblies.

The remainder of the paper is organized as follows. Section 2 presents the construction of the ROM, Section 3 describes the data-driven identification framework based on PCA-generated contact patterns and the k-NN algorithm. Section 4 presents the experimental campaign carried out on the individual components, the disk–one-blade assembly, and the full-bladed disk. Section 5 describes the FEM and validates the ROM. Section 6 details the construction of the identification dataset and the selection of the most sensitive modal features. Section 7 presents the identification results and their validation, while Section 8 discusses the main limitations of the proposed approach. Finally, Section 9 summarizes the main conclusions of the work.

2. ROM Construction

The method proposed in this section is developed for the construction of a ROM of a bladed disk assembly in the presence of mistuning induced by uncertainties in the contact at the blade–disk interface and by blade-to-blade variability. The FEM used in the reduction process consists of a disk and a blade that are not mutually constrained (Figure 1).

In general, the disk substructure can be represented starting from a single sector, i.e., a disk sector, and the full disk is then obtained by the assembly of N substructures. This approach is commonly adopted when the full disk FEM has a large number of DOFs, making direct reduction computationally expensive. In the present case, however, the size of the full disk model allows for direct reduction. Therefore, the sector-based representation is not used, and the full disk is reduced directly. Blade mistuning is subsequently introduced at the level of the blade substructures, while contact mistuning is incorporated at the blade–disk interface within the ROM, as will be discussed in Section 2.3.

For clarity, the DOFs of both the disk and the blade are partitioned as shown in Figure 1. For each component, the DOFs are divided into two groups: boundary and excess DOFs. In particular:

- The boundary DOFs correspond to the interface between substructures and the accessory DOFs. For the disk, $\boldsymbol{x}_b^D$ includes the DOFs at the left and right blade–disk contact interfaces belonging to the disk slot, denoted as $\boldsymbol{x}_{Li}^D$ and $\boldsymbol{x}_{Ri}^D$. For the blade, $\boldsymbol{x}_b^B$ includes the interface DOFs at the blade root, denoted as $\boldsymbol{x}_{Li}^B$ and $\boldsymbol{x}_{Ri}^B$, and the accessory DOFs $\boldsymbol{x}_a^B$ that correspond to locations where external forces are applied or responses are measured. Given the conforming meshes are implemented at the interface between the substructures, and the left and right interfaces share the same topology, the sets $\boldsymbol{x}_{Li}^D$, $\boldsymbol{x}_{Ri}^D$, $\boldsymbol{x}_{Li}^B$, and $\boldsymbol{x}_{Ri}^B$ have the same size, denoted by n_i.

$$\boldsymbol{x}_b^D = \begin{Bmatrix} \boldsymbol{x}_{Li}^D \\ \boldsymbol{x}_{Ri}^D \end{Bmatrix}, \qquad \boldsymbol{x}_b^B = \begin{Bmatrix} \boldsymbol{x}_{Li}^B \\ \boldsymbol{x}_{Ri}^B \\ \boldsymbol{x}_a^B \end{Bmatrix} \tag{1}$$

- The remaining DOFs are classified as excess DOFs, denoted as $\boldsymbol{x}_e^D$ and $\boldsymbol{x}_e^B$ for the disk and the blade, respectively. Their sizes are denoted by n_e^D and n_e^B.

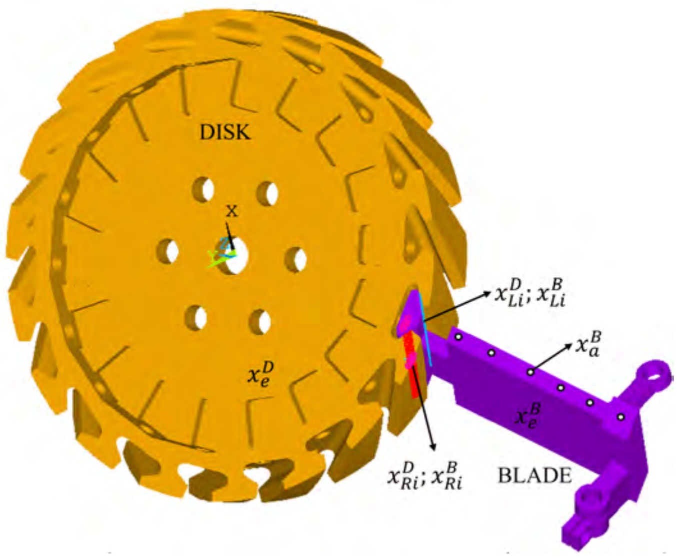

Figure 1. Schematic representation of the bladed-disk system showing the disk and blade component with the definition of interface, excess and auxiliary DOFs.

2.1. Disk Reduction

Given the partitioning introduced above, the mass and stiffness matrices of the disk can be expressed in block form as:

$$\boldsymbol{K}^D = \begin{bmatrix} \boldsymbol{K}_{ee}^D & \boldsymbol{K}_{eb}^D \\ \boldsymbol{K}_{be}^D & \boldsymbol{K}_{bb}^D \end{bmatrix}, \qquad \boldsymbol{M}^D = \begin{bmatrix} \boldsymbol{M}_{ee}^D & \boldsymbol{M}_{eb}^D \\ \boldsymbol{M}_{be}^D & \boldsymbol{M}_{bb}^D \end{bmatrix} \tag{2}$$

The disk substructure is reduced using the Craig–Bampton component mode synthesis (CB-CMS) method [31]. In this approach, the displacement field of the excess DOFs is expressed through a reduced basis that combines static and dynamic contributions. The static contribution is described by the set of constraint modes, denoted by $\boldsymbol{\Psi}_{be}$. Each constraint mode is obtained by imposing a unit displacement at one boundary DOF while keeping all other boundary DOFs fixed. The dynamic contribution is represented by a truncated set of fixed-interface normal modes, denoted by $\boldsymbol{\Phi}_{ke}$. These modes are computed by constraining all boundary DOFs and solving the associated eigenvalue problem. Only a limited number n_k of modes is retained, with $n_k \ll n_e^D$, in order to capture the dominant dynamic behavior while reducing the system size. The physical displacement vector $\boldsymbol{x}^D$ can therefore be approximated as:

$$\boldsymbol{x}^D = \begin{Bmatrix} \boldsymbol{x}_e^D \\ \boldsymbol{x}_b^D \end{Bmatrix} = \begin{bmatrix} \boldsymbol{\Phi}_{ke}^D & \boldsymbol{\Psi}_{be}^D \\ \boldsymbol{0}_{bk} & \boldsymbol{I}_{bb} \end{bmatrix} \begin{Bmatrix} \boldsymbol{\eta}_k^D \\ \boldsymbol{x}_b^D \end{Bmatrix} = \boldsymbol{R}_{CB}^D\, \boldsymbol{q}_{CB}^D \tag{3}$$

where $\boldsymbol{R}_{CB}^D$ is the CB reduction matrix, and $\boldsymbol{\eta}_k^D$ is the vector of modal amplitudes associated with the retained fixed-interface normal modes. The vector $\boldsymbol{q}_{CB}^D = \{(\boldsymbol{x}_b^D)^T\ (\boldsymbol{\eta}_k^D)^T\}^T$ thus represents the reduced generalized coordinate vector in the CB formulation.

The reduction basis $\boldsymbol{R}_{CB}^D$ is then used to project the full mass and stiffness matrices, $\boldsymbol{M}^D$ and $\boldsymbol{K}^D$, onto the reduced space, yielding the reduced matrices $\tilde{\boldsymbol{M}}^D$ and $\tilde{\boldsymbol{K}}^D$.

$$\tilde{\boldsymbol{K}}^D = (\boldsymbol{R}_{CB}^D)^T \boldsymbol{K}^D \boldsymbol{R}_{CB}^D = \begin{bmatrix} \boldsymbol{\Lambda}^D & \boldsymbol{0} \\ \boldsymbol{0} & \boldsymbol{\kappa}_{bb}^D \end{bmatrix} \tag{4}$$

$$\tilde{\boldsymbol{M}}^D = (\boldsymbol{R}_{CB}^D)^T \boldsymbol{M}^D \boldsymbol{R}_{CB}^D = \begin{bmatrix} \boldsymbol{I}_k & (\boldsymbol{\mu}_{be}^D)^T \\ \boldsymbol{\mu}_{be}^D & \boldsymbol{\mu}_{bb}^D \end{bmatrix} \tag{5}$$

$$\begin{aligned} \boldsymbol{\kappa}_{bb}^D &= \boldsymbol{K}_{bb}^D \cdot \boldsymbol{\Psi}_{be}^D + \boldsymbol{K}_{be}^D, \\ \boldsymbol{\mu}_{be}^D &= (\boldsymbol{\Psi}_{be}^D)^T \cdot \boldsymbol{M}_{ee}^D \cdot \boldsymbol{\Psi}_{be}^D + \boldsymbol{M}_{eb}^D \cdot \boldsymbol{\Psi}_{be}^D + \boldsymbol{M}_{be}^D, \\ \boldsymbol{\mu}_{bb}^D &= (\boldsymbol{\Psi}_{be}^D)^T \cdot (\boldsymbol{M}_{ee}^D \cdot \boldsymbol{\Psi}_{be}^D + \boldsymbol{M}_{eb}^D) + (\boldsymbol{M}_{be}^D)^T \cdot \boldsymbol{\Psi}_{be}^D + \boldsymbol{M}_{bb}^D \end{aligned} \tag{6}$$

2.2. Blade Reduction

The blade component is reduced using the Rubin free-interface method [32]. In this approach, the static contribution is represented by the residual attachment modes, denoted by $\boldsymbol{\Psi}_r$. These modes account for the portion of the static flexibility that is not captured by the retained dynamic modes and preserves the correct static response. In practice, they are obtained by subtracting the flexibility associated with the selected dynamic modes from the total static flexibility of the substructure. Further details on their computation can be found in [33]. The dynamic contribution is described by the free-interface normal modes, denoted by $\boldsymbol{\Phi}_f$. These modes are computed without imposing constraints at the interface DOFs, thus representing the free–free vibration behavior. An important advantage is that these modes can be directly related to experimentally identified modes obtained under free boundary conditions. If rigid body motions are present, an additional set of modes, $\boldsymbol{\Phi}_r$, is included in the basis to ensure completeness of the representation.

With this definition, the displacement vector of the blade can be approximated as:

$$\boldsymbol{x}^B \approx \boldsymbol{\Phi}_r^B\, \boldsymbol{\eta}_r^B + \boldsymbol{\Phi}_f^B\, \boldsymbol{\eta}_f^B + \boldsymbol{\Psi}_r^B\, \boldsymbol{g}_b^B = \begin{bmatrix} \boldsymbol{\Phi}_r^B & \boldsymbol{\Phi}_f^B & \boldsymbol{\Psi}_r^B \end{bmatrix} \begin{Bmatrix} \boldsymbol{\eta}_r^B \\ \boldsymbol{\eta}_f^B \\ \boldsymbol{g}_b^B \end{Bmatrix} = \boldsymbol{R}_R^B\, \boldsymbol{q}_R^B \tag{7}$$

where $\boldsymbol{R}_R^B$ is the Rubin reduction matrix and $\boldsymbol{q}_R^B = \{(\boldsymbol{\eta}_r^B)^T\ (\boldsymbol{\eta}_f^B)^T\ (\boldsymbol{g}_b^B)^T\}^T$ is the corresponding reduced generalized coordinate vector. The vectors $\boldsymbol{\eta}_r^B$ and $\boldsymbol{\eta}_f^B$ are the reduced set of generalized coordinates associated with the rigid body and free-interface modes, respectively, while $\boldsymbol{g}_b^B$ contains the forces acting at the boundary DOFs. By projecting the blade FE mass and stiffness matrices onto the space spanned by the columns of $\boldsymbol{R}_R^B$, the following reduced matrices are obtained:

$$\bar{\boldsymbol{M}}^B = (\boldsymbol{R}_R^B)^T \cdot \boldsymbol{M}^B \cdot \boldsymbol{R}_R^B = \begin{bmatrix} \boldsymbol{I} & \boldsymbol{0} & \boldsymbol{0} \\ \boldsymbol{0} & \boldsymbol{I} & \boldsymbol{0} \\ \boldsymbol{0} & \boldsymbol{0} & \boldsymbol{M}_{r,b}^B \end{bmatrix}, \tag{8}$$

$$\bar{\boldsymbol{K}}^B = (\boldsymbol{R}_R^B)^T \cdot \boldsymbol{K}^B \cdot \boldsymbol{R}_R^B = \begin{bmatrix} \boldsymbol{0} & \boldsymbol{0} & \boldsymbol{0} \\ \boldsymbol{0} & \boldsymbol{\Omega}_f^2 & \boldsymbol{0} \\ \boldsymbol{0} & \boldsymbol{0} & \boldsymbol{G}_{r,b}^B \end{bmatrix} \tag{9}$$

where $\boldsymbol{M}_{r,b}^B$ and $\boldsymbol{G}_{r,b}^B$ are the interface inertia and flexibility associated with the residual flexibility modes at the boundary. These can be written as:

$$\boldsymbol{G}_{r,b}^B = (\boldsymbol{\Psi}_r^B)^T \cdot \boldsymbol{K}^B \cdot \boldsymbol{\Psi}_r^B, \qquad \boldsymbol{M}_{r,b}^B = (\boldsymbol{\Psi}_r^B)^T \cdot \boldsymbol{M}^B \cdot \boldsymbol{\Psi}_r^B \tag{10}$$

The reduced matrices obtained with the Rubin free-interface approach possess a clear and physically interpretable structure. As expressed in Equation (9), the reduced blade stiffness matrix $\bar{\boldsymbol{K}}^B$ contains a diagonal block with the squared free-interface natural frequencies, $\boldsymbol{\Omega}_f^2$, which is independent of the choice of boundary DOFs.

The Rubin reduction does not directly provide a standard super-element formulation, as the boundary DOFs are expressed in terms of interface forces $\boldsymbol{g}_b^B$ rather than interface displacements $\boldsymbol{x}_b^B$. Therefore, an additional transformation is required to express the boundary DOFs in terms of displacements [34]. Such a transformation is found by pre-multiplying Equation (7) by the boolean matrix $\boldsymbol{A}$, which selects boundary DOFs $\boldsymbol{x}_b^B$ from the full displacement vector $\boldsymbol{x}^B$:

$$\boldsymbol{x}_b^B = \boldsymbol{A}\boldsymbol{x}^B = \boldsymbol{A}(\boldsymbol{\Phi}_r^B \boldsymbol{\eta}_r^B + \boldsymbol{\Phi}_f^B \boldsymbol{\eta}_f^B + \boldsymbol{\Psi}_r^B \boldsymbol{g}_b^B) \tag{11}$$

From this equation, the boundary force DOFs can be expressed as:

$$\boldsymbol{g}_b^B = \boldsymbol{K}_{r,b}^B(\boldsymbol{x}_b^B - \boldsymbol{A}\boldsymbol{\Phi}_r^B\boldsymbol{\eta}_r^B - \boldsymbol{A}\boldsymbol{\Phi}_f^B\boldsymbol{\eta}_f^B) \tag{12}$$

In this expression, $\boldsymbol{K}_{r,b}^B$ is the residual stiffness corresponding to the boundary DOFs, which can be obtained by applying the matrix $\boldsymbol{A}$ to the residual flexibility matrix, i.e., matrix of residual attachment modes, and taking inverse:

$$\boldsymbol{K}_{r,b}^B = \left(\boldsymbol{A} \cdot \boldsymbol{\Psi}_r^B\right)^{-1} \tag{13}$$

Therefore, the secondary transformation can be expressed as:

$$\begin{Bmatrix} \boldsymbol{\eta}_r^B \\ \boldsymbol{\eta}_f^B \\ \boldsymbol{g}_b^B \end{Bmatrix} = \begin{bmatrix} \boldsymbol{I} & \boldsymbol{0} & \boldsymbol{0} \\ \boldsymbol{0} & \boldsymbol{I} & \boldsymbol{0} \\ -\boldsymbol{K}_{r,b}^B\boldsymbol{A}\boldsymbol{\Phi}_r^B & -\boldsymbol{K}_{r,b}^B\boldsymbol{A}\boldsymbol{\Phi}_f^B & \boldsymbol{K}_{r,b}^B \end{bmatrix} \begin{Bmatrix} \boldsymbol{\eta}_r^B \\ \boldsymbol{\eta}_f^B \\ \boldsymbol{x}_b^B \end{Bmatrix} = \boldsymbol{T}_2^B \begin{Bmatrix} \boldsymbol{\eta}_r^B \\ \boldsymbol{\eta}_f^B \\ \boldsymbol{x}_b^B \end{Bmatrix} \tag{14}$$

The final reduced mass and stiffness matrices can be obtained from the subsequent application of the reduction steps described from Equation (9) to Equation (14):

$$\tilde{\boldsymbol{M}}^B = (\boldsymbol{T}_2^B)^T \cdot \bar{\boldsymbol{M}}^B \cdot \boldsymbol{T}_2^B, \qquad \tilde{\boldsymbol{K}}^B = (\boldsymbol{T}_2^B)^T \cdot \bar{\boldsymbol{K}}^B \cdot \boldsymbol{T}_2^B \tag{15}$$

$$\tilde{\boldsymbol{M}}^B = \begin{bmatrix} \boldsymbol{I} + (\boldsymbol{\Phi}^B_{r|b})^T\, \hat{\boldsymbol{M}}^B_r\, \boldsymbol{\Phi}^B_{r|b} & (\boldsymbol{\Phi}^B_{r|b})^T\, \hat{\boldsymbol{M}}^B_r\, \boldsymbol{\Phi}^B_{f|b} & -(\boldsymbol{\Phi}^B_{r|b})^T\, \hat{\boldsymbol{M}}^B_r \\ (\boldsymbol{\Phi}^B_{f|b})^T\, \hat{\boldsymbol{M}}^B_r\, \boldsymbol{\Phi}^B_{r|b} & \boldsymbol{I} + (\boldsymbol{\Phi}^B_{f|b})^T\, \hat{\boldsymbol{M}}^B_r\, \boldsymbol{\Phi}^B_{f|b} & -(\boldsymbol{\Phi}^B_{f|b})^T\, \hat{\boldsymbol{M}}^B_r \\ -\hat{\boldsymbol{M}}^B_r\, \boldsymbol{\Phi}^B_{r|b} & -\hat{\boldsymbol{M}}^B_r\, \boldsymbol{\Phi}^B_{f|b} & \hat{\boldsymbol{M}}^B_r \end{bmatrix} \tag{16}$$

$$\tilde{\boldsymbol{K}}^B = \begin{bmatrix} (\boldsymbol{\Phi}^B_{r|b})^T\, \boldsymbol{K}^B_{r,b}\, \boldsymbol{\Phi}^B_{r|b} & (\boldsymbol{\Phi}^B_{r|b})^T\, \boldsymbol{K}^B_{r,b}\, \boldsymbol{\Phi}^B_{f|b} & -(\boldsymbol{\Phi}^B_{r|b})^T\, \boldsymbol{K}^B_{r,b} \\ (\boldsymbol{\Phi}^B_{f|b})^T\, \boldsymbol{K}^B_{r,b}\, \boldsymbol{\Phi}^B_{r|b} & \boldsymbol{\Omega}^2_f + (\boldsymbol{\Phi}^B_{f|b})^T\, \boldsymbol{K}^B_{r,b}\, \boldsymbol{\Phi}^B_{f|b} & -(\boldsymbol{\Phi}^B_{f|b})^T\, \boldsymbol{K}^B_{r,b} \\ -\boldsymbol{K}^B_{r,b}\, \boldsymbol{\Phi}^B_{r|b} & -\boldsymbol{K}^B_{r,b}\, \boldsymbol{\Phi}^B_{f|b} & \boldsymbol{K}^B_{r,b} \end{bmatrix} \tag{17}$$

where $\hat{\boldsymbol{M}}^B_r = (\boldsymbol{K}^B_{r,b})^T \cdot \boldsymbol{M}^B_{r,b} \cdot \boldsymbol{K}^B_{r,b}$ is the condensed residual inertia matrix associated with the residual flexibility modes at the interface. $\boldsymbol{\Phi}^B_{r|b} = \boldsymbol{A} \cdot \boldsymbol{\Phi}^B_r$ and $\boldsymbol{\Phi}^B_{f|b} = \boldsymbol{A} \cdot \boldsymbol{\Phi}^B_f$ denote the partitions of the rigid body and free-interface modes related to the boundary DOFs.

2.3. Mistuning Modeling

In the proposed framework, mistuning is treated as the combination of two distinct contributions: blade mistuning and contact mistuning. Blade mistuning arises from variability among the blades, which is reflected in variations of their natural frequencies. Under the assumption of small mistuning, blade mistuning is modeled as a perturbation of the square of the blade natural frequencies (eigenvalues) under free–free boundary conditions. Contact mistuning arises from the variation of the contact topology at the blade–disk interface. In an ideal configuration, the contact is uniformly distributed over the interface. In practice, due to manufacturing tolerances, surface roughness, and other sources of variability, the actual contacting regions differ from one slot to another. These variations define the contact mistuning in the present framework.

2.3.1. Blade Mistuning

In the present framework, blade mistuning is introduced by acting directly on the modal properties of the blade component. In particular, the variability is modeled through modifications of the free-interface eigenvalues, which correspond to the diagonal entries of the matrix $\boldsymbol{\Omega}^2_f$ in Equation (17). This choice allows the ROM to be updated without redefining the reduction basis. Since the perturbations are applied only to the retained natural frequencies, the structure of the reduced matrices remains unchanged, and the formulation preserves a clear analytical form. The approach is based on the assumption that mistuning does not significantly alter the mode shapes of the mistuned substructure, which are therefore taken as identical to those of the tuned configuration. In addition, the disk is assumed to be nominally tuned, so that all variability is attributed to the blades. As a result, the variability between blades are entirely described by changes in their natural frequencies. This modeling strategy is particularly suitable for experimental applications, as the required modal information can be obtained from free–free tests and directly introduced into the ROM.

In the reduced stiffness matrix (Equation (17)), the blade free-interface natural frequencies appear explicitly in the diagonal block, corresponding to the (2,2) partition of the matrix:

$$\boldsymbol{\Omega}^2_f = \mathrm{diag}\left(\omega^2_{f,1},\ \omega^2_{f,2},\ \ldots,\ \omega^2_{f,m}\right) \tag{18}$$

where $\omega_{f,i}$ denotes the i-th free-interface natural frequency of the blade, and m is the number of retained free-interface modes in the reduction basis.

In an ideally tuned configuration, all blades share identical dynamic properties, leading to identical reduced stiffness matrices and free-interface natural frequencies. In real structures, mistuning introduces variations in these quantities from blade to blade. Accordingly, the eigenvalue matrix of the j-th perturbed blade can be expressed as

$$(\boldsymbol{\Omega}_f^{(j)})^2 = \mathrm{diag}\Big(\omega_{f,1}^2(1+\delta_1^{(j)}),\ \omega_{f,2}^2(1+\delta_2^{(j)}),\ \ldots,\ \omega_{f,m}^2(1+\delta_m^{(j)})\Big), \tag{19}$$

where $\delta_i^{(j)}$ represents the relative perturbation (i.e., mistuning parameter) associated with the i-th free-interface mode of the j-th blade.

The proposed approach allows a high degree of flexibility, as each blade can be characterized by a distinct set of mistuning parameters, with independent perturbations applied to the retained modes. In a numerical application, these perturbations can be directly obtained from numerical modal analyses of the blade components by extracting their natural frequencies. In experimental applications, however, the number of modes that can be considered is constrained by the subset of free-interface modes that can be reliably identified from measurements.

2.3.2. Contact Mistuning

In the present framework, contact mistuning is modeled as variations in the contact topology at the blade–disk interface. This requires distinguishing, for both the blade and the disk, between interface nodes that are in contact and those that are not. Accordingly, the boundary DOFs of each substructure are partitioned into contacting and detached sets, leading to the following representation:

$$\boldsymbol{x}_b^D = \begin{Bmatrix} \boldsymbol{x}_{Li,c}^D \\ \boldsymbol{x}_{Ri,c}^D \\ \boldsymbol{x}_{Li,d}^D \\ \boldsymbol{x}_{Ri,d}^D \end{Bmatrix}, \qquad \boldsymbol{x}_b^B = \begin{Bmatrix} \boldsymbol{x}_{Li,c}^B \\ \boldsymbol{x}_{Ri,c}^B \\ \boldsymbol{x}_{Li,d}^B \\ \boldsymbol{x}_{Ri,d}^B \\ \boldsymbol{x}_a^B \end{Bmatrix} \tag{20}$$

where the subscripts c and d denote interface DOFs corresponding to contacting and detached nodes, respectively. This partitioning enables the enforcement of constraints exclusively on the DOFs associated with contacting nodes during the assembly of the bladed disk.

2.4. Contact Modeling and Bladed Disk Assembly

The assembly of the bladed disk requires the modeling of the contact at the blade–disk interface. In general, this can be addressed using different strategies, such as penalty-based formulations, nonlinear frictional models, or simplified compatibility-based approaches. In the present framework, a linear analysis framework is considered, focusing on the identification of natural frequencies and mode shapes; thus, contact nonlinearities and friction effects are assumed to have a negligible influence on the response. Based on this assumption, a simplified modeling strategy is adopted, in which contact is enforced through node-to-node compatibility conditions. Specifically, the DOFs of the contacting nodes on the blade and disk are directly coupled, imposing displacement continuity at the interface. This approach avoids the introduction of additional contact elements and preserves a linear formulation. Consequently, only the nodes belonging to the coincident contacting regions of the blade and disk are involved in the assembly process.

The full-bladed-disk ROM is obtained by imposing compatibility between the interface DOFs corresponding to the contacting nodes on both the left and right sides of the blade and disk substructures, i.e., $\boldsymbol{x}^D_{Li,c}$ and $\boldsymbol{x}^B_{Li,c}$; $\boldsymbol{x}^D_{Ri,c}$ and $\boldsymbol{x}^B_{Ri,c}$. The corresponding constraint equations become:

$$\begin{cases} \boldsymbol{x}^D_{Li,c} = \boldsymbol{x}^B_{Li,c}; \\ \boldsymbol{x}^D_{Ri,c} = \boldsymbol{x}^B_{Ri,c} \end{cases} \tag{21}$$

The assembly Boolean matrix $\boldsymbol{A}_{bd}$ is constructed based on the compatibility constraints defined above, and is used to enforce the coupling between the disk and blade substructures. This matrix maps the local DOFs of the individual components to the global set of DOFs of the assembled system. The reduced mass and stiffness matrices of the bladed disk assembly are then obtained as

$$\boldsymbol{K}^{BD} = (\boldsymbol{A}_{bd})^T \begin{bmatrix} \tilde{\boldsymbol{K}}^D & \boldsymbol{0} \\ \boldsymbol{0} & \tilde{\boldsymbol{K}}^B \end{bmatrix} \boldsymbol{A}_{bd}, \qquad \boldsymbol{M}^{BD} = (\boldsymbol{A}_{bd})^T \begin{bmatrix} \tilde{\boldsymbol{M}}^D & \boldsymbol{0} \\ \boldsymbol{0} & \tilde{\boldsymbol{M}}^B \end{bmatrix} \boldsymbol{A}_{bd} \tag{22}$$

3. Data-Driven Identification of Contact Patterns

This study is motivated by previous experimental observations [26,28], which showed that contact patterns measured at the blade–disk interface using pressure-sensitive film exhibit a high degree of similarity from slot to slot. An overview of the measured contact patterns across all blade root slots of an academic bladed disk is provided in Figure 2. The measured imprints present consistent spatial features with only minor local variations. This behavior can be attributed to the uniformity of manufacturing processes and tolerances, which lead to similar surface morphology across blade roots and disk slots. This characteristic is exploited to infer unknown contact patterns from a limited set of experimentally measured ones. Such an approach is particularly advantageous for bladed disks with a large number of blades, where direct measurement using pressure-sensitive films is time-consuming or impractical.

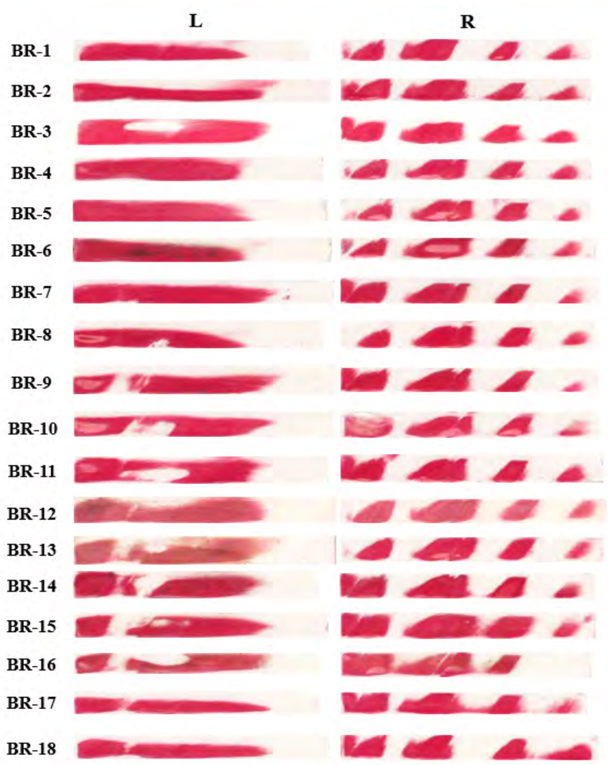

Figure 2. Measured contact patterns at the blade–disk interface for all blade root slots of the academic bladed disk. BR denotes blade–root, and the index indicates the slot number. (**L**) stands for the left slot while (**R**) for the right one.

Starting from the available measurements, a statistical representation of the contact space is constructed using PCA, allowing the extraction of its dominant features. Synthetic contact patterns are then generated by sampling within this space. Each generated pattern is combined with blade mistuning parameters and applied in a disk–one-blade model to compute the corresponding natural frequencies. In this way, a dataset is created that links contact configurations and blade variability to the modal properties of the system.

The identification of an unknown contact pattern is performed through an inverse procedure based on the k-NN algorithm. The input features consist of the natural frequencies of the assembly and blade mistuning parameters, while the output is the corresponding contact pattern. The selection is based on dynamic equivalence rather than direct spatial matching, and the set of admissible patterns is restricted to those contained in the constructed dataset.

3.1. Principal Component Analysis

PCA is employed to construct synthetic contact patterns that retain the main spatial features observed in the experimentally measured pressure-film imprints. The procedure is applied directly to the image data of the contact patterns. The generation of synthetic patterns is based on the statistical distribution of the PCA coefficients. In particular, these coefficients are assumed to follow a Gaussian distribution, which is consistent with the strong similarity and limited variability observed in the experimental measurements. Under this assumption, new contact patterns can be generated by sampling the PCA coefficients. The resulting synthetic patterns are intended to span the space of admissible contact configurations and capture its dominant characteristics.

Each pressure-film image is first converted into a grayscale matrix

$$\boldsymbol{M}^{(i)} \in \mathbb{R}^{h \times \omega}, \tag{23}$$

where h and ω denote the standardized height and width after preprocessing. Each image is then reshaped into a column vector

$$\boldsymbol{X}_i = \mathrm{vec}(\boldsymbol{M}^{(i)}) \in \mathbb{R}^d, \quad d = h \cdot \omega. \tag{24}$$

By collecting all n samples, the data matrix is formed as

$$\boldsymbol{X} = [\boldsymbol{X}_1\ \boldsymbol{X}_2\ \cdots\ \boldsymbol{X}_n]^T \in \mathbb{R}^{n \times d}. \tag{25}$$

The mean image vector is computed as

$$\boldsymbol{\mu} = \frac{1}{n}\sum_{i=1}^{n} \boldsymbol{X}_i, \tag{26}$$

and the centered data matrix is obtained by

$$\boldsymbol{X}_{\mathrm{cent}} = \boldsymbol{X} - \boldsymbol{1}\boldsymbol{\mu}^T, \tag{27}$$

where $\boldsymbol{1}$ is a column vector of ones. PCA is then performed via singular value decomposition (SVD):

$$\boldsymbol{X}_{\mathrm{cent}} = \boldsymbol{U}\boldsymbol{S}\boldsymbol{V}^T, \tag{28}$$

where $\boldsymbol{V}$ contains the principal directions (eigenvectors), $\boldsymbol{S}^2$ represents the variance, and $\boldsymbol{U}$ contains the left singular vectors. The PCA coordinates of each sample are given by

$$\boldsymbol{Z} = \boldsymbol{X}_{\mathrm{cent}}\boldsymbol{V}. \tag{29}$$

Due to the limited variability observed in the experimental data, the PCA coefficients along each principal direction are assumed to follow Gaussian distributions. Since only a limited number of experimentally measured contact patterns are available, this assumption is adopted as a practical modeling choice. For each component, the sample mean and standard deviation are computed as

$$\mu_z = \frac{1}{n}\sum_{i=1}^{n} Z_i, \qquad \sigma_z = \sqrt{\frac{1}{n-1}\sum_{i=1}^{n}(Z_i - \mu_z)^2}. \tag{30}$$

New synthetic PCA coefficient vectors are generated as

$$\kappa_z = \mu_z + \sigma_z \cdot \mathrm{Scale} \cdot r, \tag{31}$$

where r is a scalar random variable sampled from a standard normal distribution, i.e., $r \sim \mathcal{N}(0,1)$. The parameter *Scale* controls the amplitude of variability around the measured distribution.

The corresponding synthetic pattern is reconstructed as

$$\boldsymbol{X}_{\mathrm{syn}} = \boldsymbol{\mu} + \boldsymbol{V}\boldsymbol{\kappa}. \tag{32}$$

Finally, $\boldsymbol{X}_{\mathrm{syn}}$ is reshaped back into matrix form to obtain the synthetic contact pattern in grey-scale image form.

3.2. k-Nearest Neighbors Algorithm

Once the synthetic contact patterns are generated, their effect on the dynamic response of the disk–one-blade system is evaluated in terms of natural frequencies. In this framework, each sample consists of a pair of contact patterns (left and right sides of the joint) associated with the corresponding set of natural frequencies, forming a dataset that links interface conditions to the system modal parameters. This dataset is then used to perform inverse identification of unknown contact patterns from measured natural frequencies. The identification is carried out using the k-NN algorithm, which selects the contact patterns in the dataset that are closest to the measured ones in the feature space defined by the natural frequencies.

k-NN algorithm is a non-parametric classification method widely used in pattern recognition and data-driven identification [35]. Given an input feature vector, the algorithm assigns a label by comparing it with all samples in a labeled dataset and selecting the closest ones according to a chosen distance metric. The similarity between two feature vectors $\boldsymbol{x}$ and $\boldsymbol{y}$ of dimension d is evaluated using a weighted Euclidean distance:

$$d(\boldsymbol{x},\boldsymbol{y}) = \sqrt{\sum_{i=1}^{d} w_i\,(x_i - y_i)^2}, \tag{33}$$

where w_i denotes the weight associated with the i-th feature.

Once the distances are computed, the algorithm identifies the k nearest neighbors. The predicted label is then determined based on these neighbors. In the present work, the simplest case $k = 1$ is adopted, corresponding to the nearest neighbor (1-NN) classification, where the class of the closest sample is directly assigned to the input.

In this framework, the k-NN algorithm is used to identify the unknown contact pattern at the blade–disk joint based solely on modal information, i.e., natural frequencies. Each contact configuration in the dataset generates a corresponding vector of natural frequencies:

$$\boldsymbol{f}_j = \begin{Bmatrix} f_{j,1} \\ f_{j,2} \\ \vdots \\ f_{j,m} \end{Bmatrix}, \qquad j = 1, \ldots, N, \tag{34}$$

where m is the number of modes and N is the total number of samples.

These vectors form the labeled dataset, where the labels define the contact patterns. For an unknown contact condition, a modal analysis of the disk–one-blade system is performed, yielding a frequency vector $\boldsymbol{f}^*$. The distance between $\boldsymbol{f}^*$ and each dataset sample is computed as

$$d_j = d(\boldsymbol{f}^*, \boldsymbol{f}_j). \tag{35}$$

The identified contact pattern is obtained by selecting the sample that minimizes this distance:

$$j^* = \arg\min_j d_j. \tag{36}$$

The selected pattern represents the dynamically closest match within the dataset. Although the identified pattern may not exactly coincide with the true contact distribution, it provides the nearest dynamically equivalent approximation in the considered dataset.

4. Experimental Campaign

This section describes the experimental activity carried out to characterize the individual components (blade and disk), the disk–one-blade assembly, and the full-bladed disk. The characterization of the standalone components is used to calibrate the corresponding FEM and to identify the blade mistuning parameters, i.e., perturbations of the system eigenvalues. These parameters are subsequently introduced into the ROM to construct an offline digital twin of the bladed disk based on experimental data.

The disk–one-blade configuration is tested to extract the natural frequencies of the assembly, which are used as input for the contact identification procedure. Finally, the full-bladed disk is tested to validate the proposed methodology, by comparing the measured modal parameters with the numerical predictions obtained using the identified contact patterns.

The test specimen is an academic bladed disk designed for laboratory investigations. The assembly consists of an 18-blade disk with a disk diameter of 200 mm, a blade length of 117.5 mm, and an overall assembled diameter of 412 mm. All tests are performed under free–free boundary conditions by supporting the components on soft foam, whose stiffness is assumed negligible. Excitation is applied using an impact hammer equipped with a load cell on tip to measure the input force, while the response is measured using a laser Doppler vibrometer (LDV), specifically the Polytec PSV-500 system. The acquired signals are processed by the data acquisition system to obtain frequency response functions (FRF). These are subsequently analyzed through experimental modal analysis (EMA), using the Least Squares Rational Fraction (LSRF) method to identify natural frequencies and mode shapes. Figure 3 shows the experimental setup employed for the modal testing, including the LDV system, the impact hammer, and the data acquisition hardware.

Figure 3. Experimental setup used for modal testing under free–free conditions, showing the LDV system, impact hammer, and data acquisition hardware.

4.1. Component Testing

Figure 4 shows the components under investigation, the disk (Figure 4a) and a representative blade (Figure 4b). The total number of blades for a given setup is 18, and they are not perfectly identical. In addition to variations induced by manufacturing tolerances, blade-to-blade differences arise from specific geometric features, such as the presence or absence of fillets at certain edges. These geometric variations introduce an additional source of mistuning. However, these differences do not affect the modal content of the blades. All blades exhibit the same set of modes within the considered frequency range, and the corresponding mode shapes show similar spatial distributions. The effect of these geometric variations is therefore solely reflected in shifts of the natural frequencies.

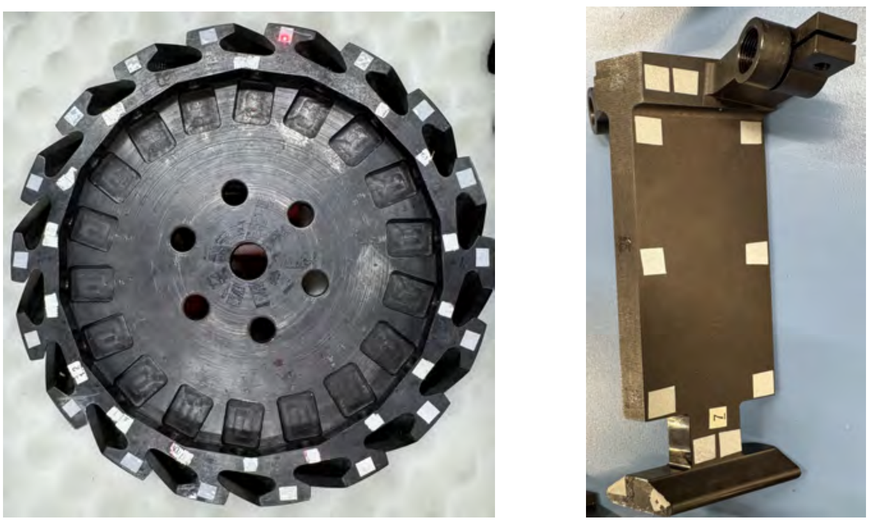

(**a**) (**b**)

Figure 4. Components under investigation: (**a**) disk; (**b**) blade.

An example of the measured FRF for both the disk and a representative blade, obtained at a selected measurement point, is shown in Figure 5. The measurements are performed in the direction orthogonal to the surface of the components, corresponding to the out-of-plane DOF.

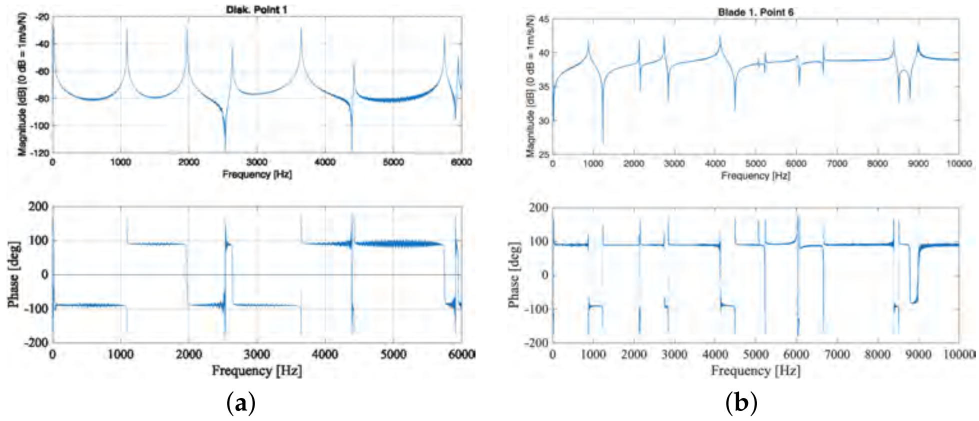

Figure 5. Measured frequency response functions (FRFs) for (**a**) the disk and (**b**) a blade at representative points.

By repeating the acquisition over all measurement points, the modal parameters are identified by processing the frequency-domain data using the LSRF EMA technique [36]. To distinguish physical modes from spurious numerical poles, a stabilization diagram is exploited by performing the identification over increasing model orders. Poles that remain stable in terms of frequency, damping, and mode shape are retained as physical modes. As a result, 11 modes are consistently identified for all blades and 7 modes for the disk within the considered frequency bandwidth.

The identified natural frequencies for the disk are reported in Table 1. Since only one acquisition point per sector was considered, and measurements were performed in the out-of-plane direction, the mode shapes can be characterized only in terms of nodal diameters.

Table 1. Identified natural frequencies and corresponding nodal diameters of the disk.

Mode	Frequency [Hz]	Nodal Diameter
1	1090.6	2
2	1971.1	0
3	2638.1	3
4	3647.6	1
5	4421.5	4
6	5747.6	2
7	5947.9	0

The identification results for the blade components are expressed in terms of the relative deviation of the squared natural frequencies with respect to their mean value across all 18 blades. This quantity is defined as

$$\delta_i^{(j)}\% = \frac{\left(\omega_{f,i}^{(j)}\right)^2 - \langle \omega_{f,i}^2 \rangle}{\langle \omega_{f,i}^2 \rangle} \cdot 100\%, \tag{37}$$

where $\langle \omega_{f,i}^2 \rangle$ denotes the mean value of the i-th free-interface eigenvalue over all blades, and $\omega_{f,i}^{(j)}$ is the corresponding frequency of the j-th blade. This representation is convenient, as it directly provides the perturbations in percentage used to construct the mistuned ROM of the assembly (Table 2).

Table 2. Relative perturbations $\delta_i^{(j)}$ of eigenvalues (in %) for each blade and mode. Values are reported with one decimal digit.

Blade	M1	M2	M3	M4	M5	M6	M7	M8	M9	M10	M11
1	−1.0	1.0	1.3	3.2	12.9	1.7	4.2	3.8	0.7	1.2	0.3
2	0.8	0.8	2.1	−1.7	−1.1	1.8	−1.1	4.4	11.1	−1.7	0.4
3	−1.1	0.8	0.7	2.6	13.3	1.2	4.3	2.3	−1.3	0.8	−1.1
4	0.1	0.8	1.0	3.2	13.1	1.6	4.1	4.4	−1.5	1.3	0.1
5	0.4	1.4	1.2	−1.1	−1.7	0.0	−1.0	4.4	−1.3	−1.3	−1.4
6	0.0	0.9	0.5	2.0	12.8	0.7	4.0	0.8	−1.7	0.7	−1.5
7	0.0	0.3	0.3	1.0	13.2	0.3	4.4	−1.2	−1.3	0.3	−1.9
8	−1.2	0.2	0.0	1.5	12.7	0.6	3.8	0.3	−1.8	1.2	−1.3
9	0.0	0.5	1.0	1.7	15.3	1.6	4.4	0.4	0.4	1.6	0.3
10	0.1	1.4	1.2	4.1	13.0	1.4	4.8	5.7	−1.9	0.4	−1.1
11	−1.1	0.0	0.0	−1.7	−1.1	−1.2	−1.2	−1.6	−1.0	−1.8	−1.4
12	−1.1	0.9	1.3	3.4	13.5	1.4	4.7	4.4	−1.5	0.6	−1.1
13	0.5	1.8	1.8	4.2	13.0	1.8	4.8	5.7	−1.9	1.1	0.3
14	−1.1	−1.2	0.0	−1.3	12.5	0.3	3.9	−1.5	−1.4	0.6	−1.9
15	0.1	1.4	1.2	3.9	14.0	1.4	4.7	5.4	−1.2	0.3	−1.1
16	0.0	−1.6	−1.4	−1.5	−1.2	−1.3	−1.4	−1.8	−1.6	−1.0	−1.5
17	0.2	1.7	1.5	4.5	12.7	1.9	4.5	6.1	0.2	1.2	0.5
18	0.1	0.8	0.9	2.2	12.9	1.2	4.4	1.2	0.3	1.1	−1.2

4.2. Assembly Testing

The disk–one-blade assembly and the full-bladed disk configuration are shown in Figure 6. The blades are attached to the disk using two bolts symmetrically positioned on both sides of the disk rim. The bolts, inserted from the disk side, press the blade root against the slot, ensuring firm contact at the blade–disk interface. The tightening torque must be sufficiently high to guarantee stable contact conditions, limiting relative motion and slip at the interface, while at the same time, excessive torque should be avoided to prevent over-stiffening and possible plastic damage of the components and threads. To identify an appropriate torque level, preliminary tests were conducted on a disk–one-blade assembly by applying different tightening values. Based on these tests, a torque of 20 Nm was selected, as it ensures predominantly sticking conditions at the interface while avoiding plastic deformation. The same torque level was also used in the experiments with pressure-sensitive film (Figure 2) to measure the contact patterns employed in this study. The modal parameters of both configurations are identified using the same EMA procedure based on the LSRF technique.

Table 3 reports the mean values of the natural frequencies of the disk–one-blade assembly, obtained by over all 18 configurations corresponding to the different blades, for the first 10 modes. The variability of the assembly natural frequencies is significantly smaller than that observed for the standalone blade components. This is due to the coupling with the disk, which reduces the influence of blade-to-blade differences, as the global dynamics is governed by the combined behavior of both components. As can be seen, the identified modes are well separated in frequency, making them suitable as input features for the contact identification algorithm.

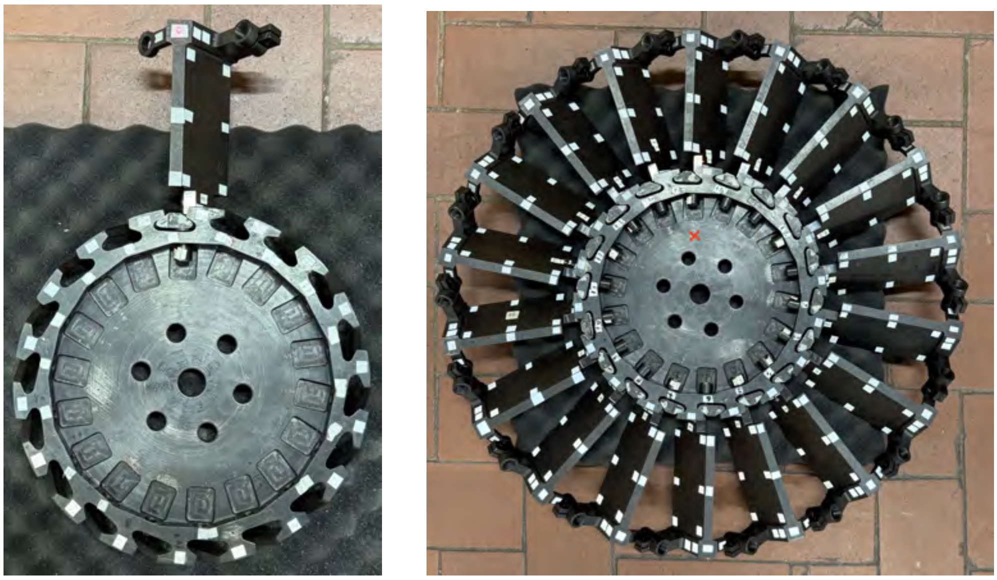

(**a**) (**b**)

Figure 6. (**a**) Disk–one-blade assembly; (**b**) full-bladed disk assembly. Red cross indicates the excitation point.

Table 3. Mean natural frequencies (Hz) of the disk–one-blade assembly for the first 10 modes. Values are reported with one significant digit.

Mode	**1**	**2**	**3**	**4**	**5**	**6**	**7**	**8**	**9**	**10**
$\bar{f}$ (Hz)	194.8	540.4	742.3	1114.7	1157	1338.5	1992	2579.3	2692.5	3174.4

The modal identification of the full-bladed disk assembly is performed using the LSRF EMA technique applied to the experimentally measured FRFs. Due to the high modal density within a unit frequency bandwidth, a local fitting strategy is adopted. In total, 82 modes are identified within the measured frequency range. The corresponding natural frequencies are graphically reported in Figure 7.

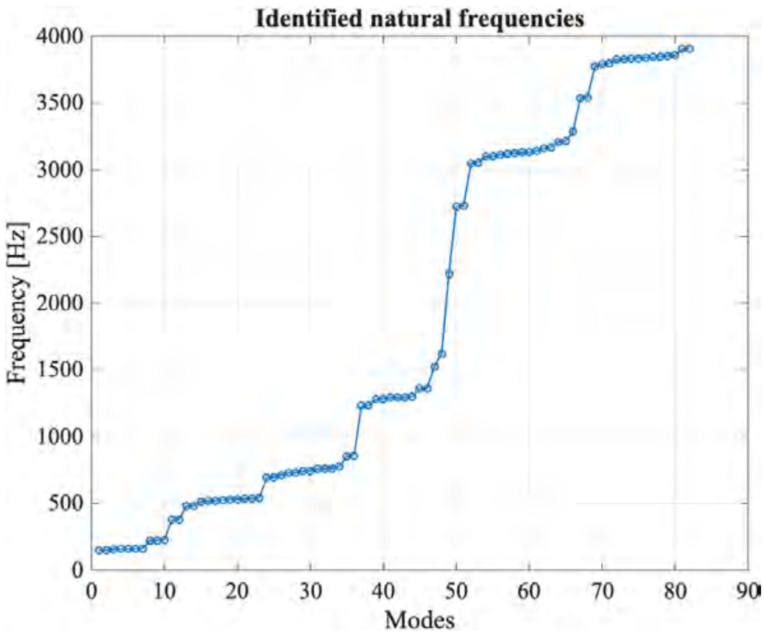

Figure 7. Identified natural frequencies of the full assembly.

5. FEM Description and ROM Validation

The numerical analysis starts with the development of FEM for the individual components, i.e., the disk and the blade. The components are meshed using SOLID186 elements, which are higher-order 3D solid elements with 20 nodes and quadratic displacement behavior. Each node has three translational DOFs along the x, y, and z directions. Special attention is devoted to the blade–disk interface, where a conforming mesh is adopted. This ensures node-to-node correspondence at the interface, facilitating the enforcement of compatibility conditions during the assembly process. The resulting FE models of the disk and blade are shown in Figure 8.

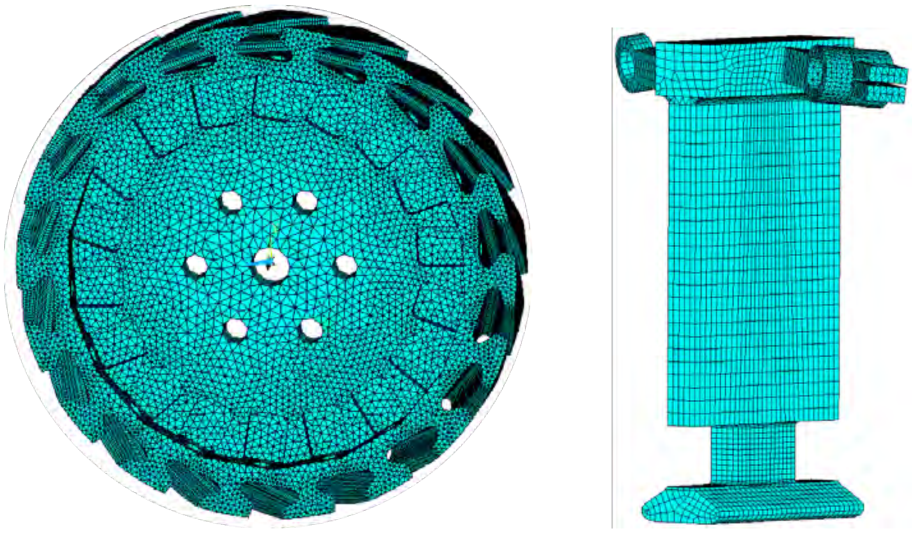

(**a**) (**b**)

Figure 8. FE model of the components under investigation: (**a**) disk; (**b**) blade.

Both components are made of the same material, namely quenched and tempered C40 steel (EN 10083-2, grade C40) [37]. The material properties of the FE models are calibrated based on experimental measurements. Two parameters are adjusted: the density and the Young modulus. The density of the disk is computed from the ratio between the measured mass of the component and its CAD volume. For the blades, the density is evaluated using the mean mass across all 18 specimens. For the disk, the Young modulus is calibrated by matching the first natural frequency of the FE model to the experimentally identified value of 1090.6 Hz. For the blade, the calibration is performed by matching the first eigenvalue of the FE model with the mean of the squared value of the experimentally identified first natural frequency. This choice is consistent with the mistuning modeling strategy, where perturbations are introduced in the eigenvalue matrix of the blade ROM (see Equation (19)) with zero mean. As a result, the calibrated model avoids introducing a systematic bias. The final values of the calibrated density and Young's modulus for both components are reported in Table 4.

Table 4. Calibrated material parameters of the components.

Component	Density [kg/m^3]	Young Modulus [GPa]
DISK	7864.6	202
BLADE	7832.5	212

Figure 9a shows the validation of the disk FE model by comparing the natural frequencies obtained from the FEM with the experimental measurements (see Figure 9). Very good agreement is observed, with errors remaining below 2% for all identified modes. Figure 9b presents the validation of the blade FE model. Due to space limitations, legends are not reported; in the upper plot, dashed lines correspond to numerical results, while solid lines represent the experimental frequencies of the 18 blades. A slightly larger discrepancy is observed for mode 5, which is characterized by deformation concentrated at the top flank, where the presence of the fillet strongly influences the local stiffness. In the FEM, the fillet geometry is slightly simplified to avoid excessively refined and impractical mesh regions. As a result, the stiffness of this region is slightly underestimated, leading to lower predicted natural frequencies. Overall, a good agreement is observed across all modes.

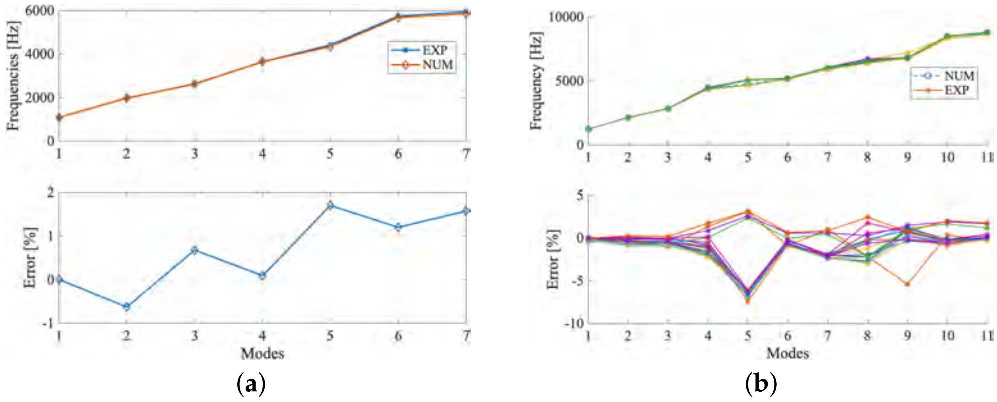

Figure 9. (**a**) Validation of the disk FE model; (**b**) validation of the blade FE model through comparison of natural frequencies.

The next step consists in constructing ROM of the individual components. The disk is reduced using the Craig–Bampton fixed-interface method, while the blade is reduced using the Rubin free-interface approach, which enables the introduction of mistuning through perturbations of the free-interface natural frequencies. A total of 300 fixed-interface modes are retained for the disk and 50 free-interface modes for the blade. These values are selected as a trade-off between the accuracy of the ROM and the size of the substructures. For the disk, the boundary DOFs retained during the reduction include contact interface DOFs at the blade–disk and bolt–blade interfaces for each slot. For the blade, the retained DOFs correspond to the same interface nodes, along with three additional measurement nodes used in the experimental campaign. The sizes of the FE models prior to reduction are illustrated in Table 5. The reduction process results in significant compression, with a reduction of approximately 99.3% for the blade model and 98.6% for the disk model sizes.

Table 5. DOFs of the FEM prior to reduction.

Component	**DOFs**
Disk – excess	2,177,277
Disk – disk–blade interface (per slot)	1302
Disk – bolt–blade interface (per slot)	306
Disk – accessory	54
Disk – total	**2,206,275**
Blade – excess	229,989
Blade – blade–disk interface	1302
Blade – blade–bolt interface	306
Blade – accessory	9
Blade – total	**231,606**

The modal characteristics of each substructure are obtained by solving the generalized eigenvalue problem:

$$\left(\mathbf{K} - \omega^2\mathbf{M}\right)\boldsymbol{\phi} = \mathbf{0}, \tag{38}$$

where $\mathbf{K}$ and $\mathbf{M}$ are the stiffness and mass matrices, respectively, ω is the natural frequency, and $\boldsymbol{\phi}$ is the corresponding mode shape. The accuracy of the reduced-order models is assessed by comparing the natural frequencies of the substructures obtained from the ROM with those of the corresponding FEM, for both the disk (Figure 10a) and the blade (Figure 10b). As can be seen, the ROM of both substructure exhibits an excellent agreement with the FEM over the considered modes. The relative error remains very low, generally below 0.3%, indicating that the selected number of retained modes ensures a highly accurate representation of the system dynamics.

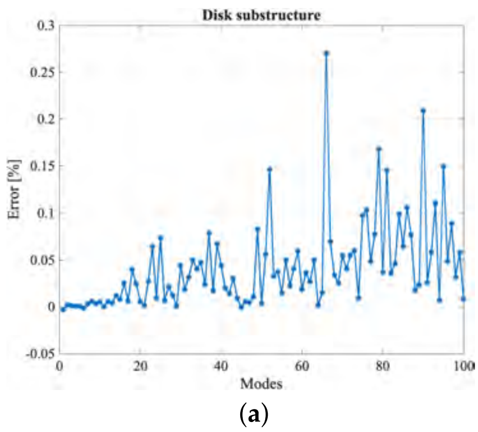

Figure 10. Validation of reduced-order models: (**a**) disk substructure; (**b**) blade substructure (relative error in natural frequencies).

Before validating the mistuned ROM against the experimental results, the contact modeling must be defined. The experimentally observed contact patterns obtained from pressure-sensitive film (Figure 2) are first converted into a set of contacting nodes. To this end, an image processing procedure is applied. The contact interface in numerical model is discretized by a regular grid of nodes arranged in a 7×31 layout, which is superimposed onto the pressure-film image. A threshold on the color intensity is then introduced to distinguish between contact and non-contact regions. Grid points with intensity above the threshold are classified as contacting nodes, while the others are considered detached. The resulting contact grid for a representative blade–root joint (BR-17) is shown in Figure 11.

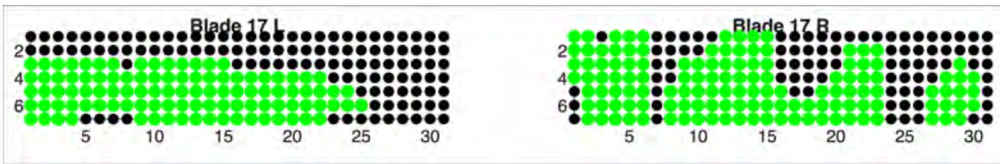

Figure 11. The resulting contact grid after the image post-processing.

In addition, a minor modification is introduced in the FE model to account for the presence of the tightening bolts. Specifically, the bolts are modeled as additional components with the same geometry and are positioned at the fixture locations. This approach allows for a more accurate representation of the mass contribution of the bolts compared to a simplified lumped mass assumption, for which the exact position of the center of mass would be difficult to determine. Another contact region, i.e., the interface between the blade and the bolt, along which the preload is transmitted to secure the blade within the disk slot, is also modeled. In this case, a simple node coupling approach is adopted by enforcing compatibility conditions at the corresponding nodes.

The validation of the disk–single blade assembly in the presence of contact and blade mistuning is performed by comparing the natural frequencies (Figure 12a) and the mode shapes (Figure 12b) obtained from the mistuned ROM and the experiments for the assembly with representative blade. The mode shape comparison is carried out using the accessory DOFs retained during the blade reduction procedure. In particular, three out-of-plane displacement DOFs corresponding to the z-direction of the numerical model are selected at the blade leading edge to define the experimental and numerical mode shapes. The natural frequencies show excellent agreement, where the difference between two doesn't exceed 1%. The MAC values as well are generally high, indicating a strong correlation of the mode shapes. This trend remains consistent across the assembly with any blade.

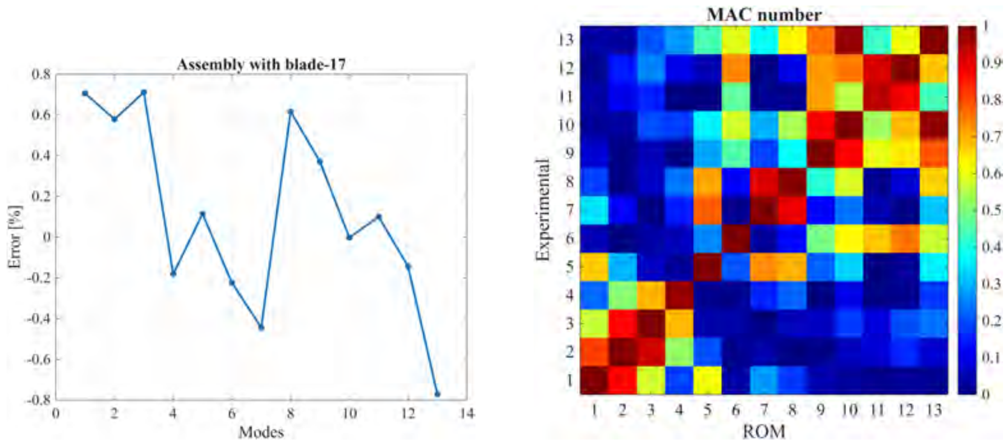

(**a**) (**b**)

Figure 12. Validation of the disk–single blade assembly: (**a**) natural frequencies comparison; (**b**) MAC matrix between numerical and experimental mode shapes.

The validation of the mistuned ROM for the full-bladed disk is performed in a similar manner. Due to the high modal density, not all numerical modes can be directly matched with experimental ones. Therefore, the correspondence between numerical and experimental modes is established using a MAC-based criterion within a local frequency neighborhood. The mode shapes of the full assembly are constructed using the same three out-of-plane displacement DOFs retained for each blade at the leading edge, resulting in a total of $18 \times 3 = 54$ DOFs defining the mode shape vectors of the complete assembly. The comparison of natural frequencies (Figure 13a) shows a good overall agreement, with most errors remaining within a small range. Larger deviations are observed only for a limited number of modes. The MAC matrix (Figure 13b) exhibits a clear diagonal trend, indicating a strong correlation between numerical and experimental mode shapes. Overall, the results confirm that the proposed mistuned ROM provides an accurate representation of the dynamic behavior of the full assembly.

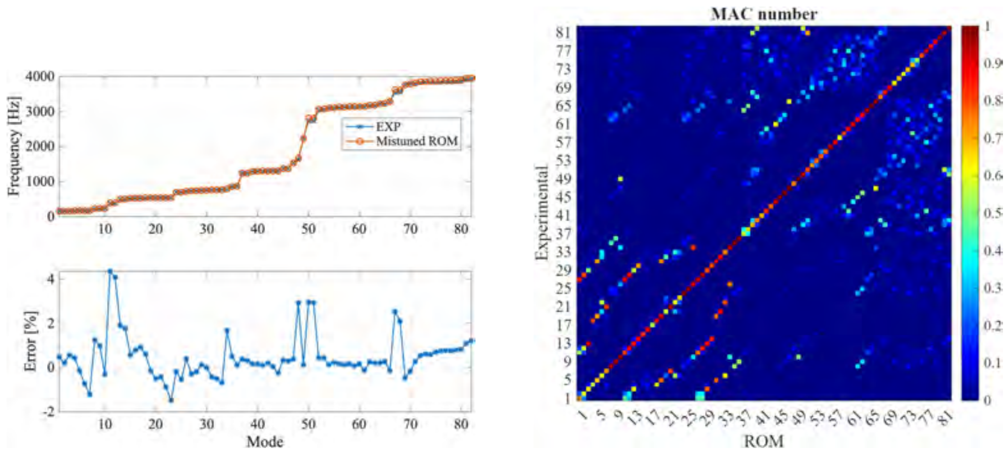

(**a**) (**b**)

Figure 13. (**a**) Comparison of natural frequencies between experiment and mistuned ROM and corresponding error; (**b**) MAC between experimental and numerical mode shapes.

6. Dataset Construction for Contact Pattern Identification

Having validated the proposed ROM using the complete set of experimentally measured contact maps, the following procedure assumes that only a limited subset of these measurements is available. A synthetic dataset is therefore constructed to enable the identification of the unknown contact patterns. The development of synthetic contact patterns is motivated by the experimental observation that the contact topology at the blade–disk interface exhibits a high degree of similarity across different joints and contact sides. This suggests that the contact patterns can be described in terms of a limited number of dominant spatial features. These features are extracted from a reduced set of experimentally measured patterns using PCA (see Section 3.1). Once the PCA basis is obtained, synthetic contact patterns can be generated by sampling the corresponding coefficients independently for each contact side. For each generated pattern, a modal analysis of the disk–one-blade assembly is performed, allowing the associated set of natural frequencies to be determined. In this way, a dataset is constructed that links contact patterns to their corresponding modal signature. This dataset is then used as a prediction basis for unknown blade–root joints. Given a set of measured natural frequencies, the identification is performed by selecting the contact pattern whose associated frequency is closest in the dataset. The procedure is therefore based on dynamic equivalence, where patterns are matched according to their frequency signature rather than their spatial distribution.

6.1. PCA Sampling. Synthetic Patterns

A subset of five experimentally measured blade roots (BR-3, BR-7, BR-10, BR-14, BR-17) is used to construct the PCA basis and the associated statistical descriptors (see Section 3.1). This number is selected as a trade-off between the experimental effort required to obtain pressure-film measurements and the accuracy of the identification procedure. The selected blade roots are distributed along the disk circumference to avoid spatial bias. Synthetic contact patterns are generated by sampling the PCA coefficients (Equation (31)), independently for each contact side. A total of 10 patterns are generated for the left side and 10 for the right side, providing sufficient variability while keeping the dataset size manageable. Increasing the number of samples was found not to introduce significant difference in contact topology. Considering all possible combinations between the left- and right-side patterns results in 100 distinct contact configurations for a blade–root joint. Examples of the generated patterns in grey-scale for the left and right sides are shown in Figure 14.

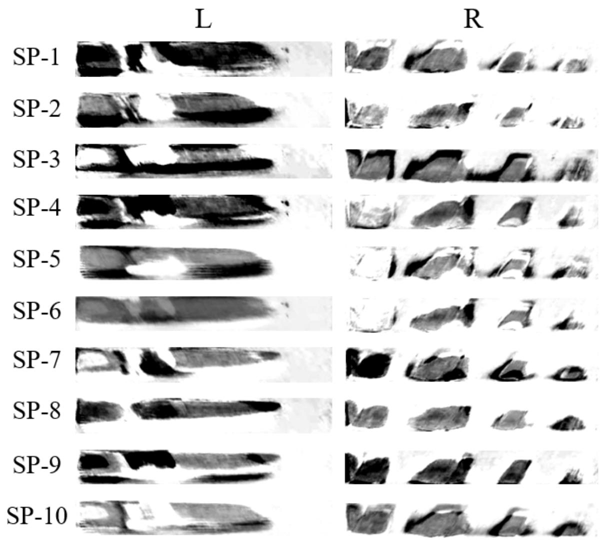

Figure 14. Synthetic contact patterns generated via PCA sampling for the left (**L**) and right (**R**) sides of the blade–disk interface. 'SP' denotes synthetic pattern.

6.2. Modal Sensitivity to Contact Mistuning

At this point, a sensitivity analysis is carried out to identify the modes that are most sensitive to contact mistuning. Since the identification procedure is based on dynamic equivalence, it is important to select modes whose natural frequencies are highly sensitive to variations in the contact topology. To this end, a numerical modal analysis is performed on the disk–one-blade ROM by imposing all 100 combinations of the synthetic contact patterns. The blade is assumed to be tuned in order to isolate the effect of contact mistuning and avoid bias due to blade variability. The sensitivity of the first 10 modes is evaluated by computing the standard deviation of their natural frequencies across all contact configurations. The results are shown in Figure 15. As observed, modes 5, 6, and 8 exhibit the highest sensitivity to contact variations. These modes are therefore selected as input features for the contact identification procedure assuming that the complete set of actual contact maps are not known. The corresponding maps are shown in Figure 16.

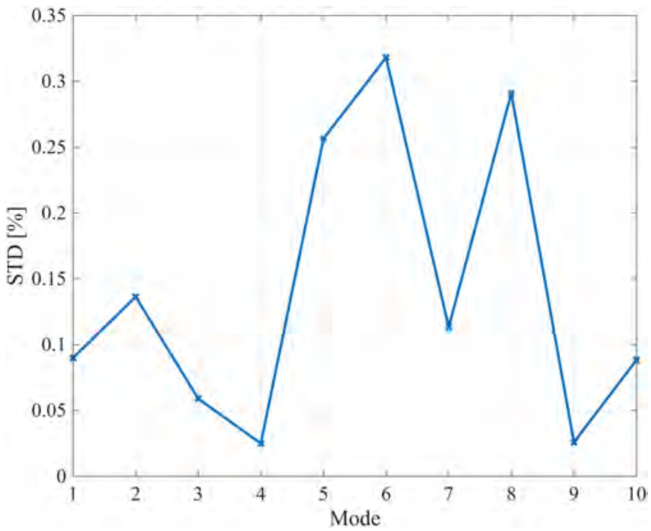

Figure 15. Standard deviation of the natural frequencies of the disk–one-blade assembly across all contact configurations, for the first 10 modes.

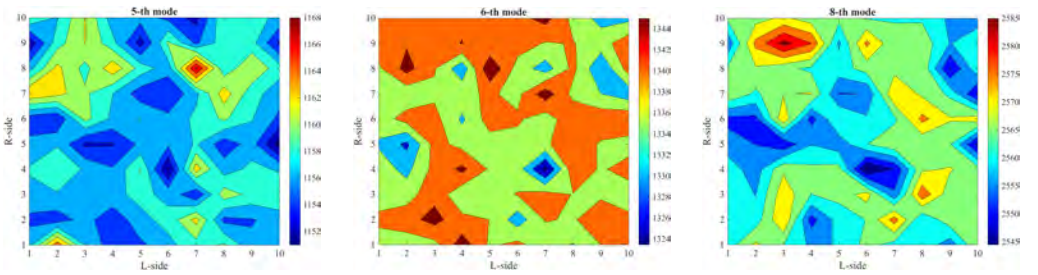

(**a**) (**b**) (**c**)

Figure 16. Natural frequency maps of the disk–one-blade assembly as a function of contact pattern. The color bars indicate the natural frequency in Hz. (**a**) 5th mode, (**b**) 6th mode, and (**c**) 8th mode. The x-axis represents the patterns on the left side (L-side), while the y-axis represents the patterns on the right side (R-side), both labeled from 1 to 10 (see Figure 14).

6.3. Dataset Construction

This section describes the construction of the dataset used in the identification framework. Since the dynamic response of a bladed disk is influenced simultaneously by both blade and contact mistuning, both effects must be included. A dataset relating only contact patterns to natural frequencies would not be representative, as the measured frequencies inherently reflect the combined contribution of both sources.

In the present framework, blade mistuning is modeled as perturbations of the system eigenvalues (see Section 2.3). Therefore, additional dimensions are introduced in the dataset to account for these perturbations, where each dimension corresponds to the variation of a specific blade mode. The number of such dimensions is selected based on the number of mistuned modes of the full-bladed disk assembly under investigation, associated with a given number of modal families of the corresponding tuned assembly. A modal family refers to a set of modes of the bladed disk assembly derived from a common blade mode, which, in the tuned assembly, appear as a sequence of system modes associated with different nodal diameters. Although this concept strictly applies to tuned systems, in the presence of small mistuning, the modal family structure is not completely lost, and the modes still exhibit a similar organization, as illustrated in Figure 7.

In this study, the mistuned modes of the full-bladed disk corresponding to the first three modal families of the tuned system are considered, leading to three dimensions associated with blade mistuning. Since each blade mode predominantly contributes to one modal family of the bladed disk, the first three blade modes define three independent blade mistuning parameters. From the experimentally identified blade perturbations (Table 2), the variations of the first three modes are observed to lie within the interval $[-0.5\%, 2\%]$. This range is discretized into six values with a step of 0.5%. Contact mistuning is described by the synthetic patterns introduced previously. Two additional dimensions are therefore included in the dataset to account for the contact mistuning, corresponding to the contact patterns on the left and right sides of the joint, each represented by a label ranging from 1 to 10. As a result, the dataset is defined by five input parameters: three related to blade mistuning and two associated with contact patterns. By considering all possible combinations, the total number of samples is $6 \times 6 \times 6 \times 10 \times 10 = 21{,}600$.

Each combination corresponds to a specific configuration of blade and contact mistuning, for which the mistuned ROM of the disk–one-blade assembly is used to compute the natural frequencies. In this work, the frequencies of the 5th, 6th, and 8th modes are retained, as identified in the previous sensitivity analysis. Therefore, the dataset establishes a mapping between five input parameters (causes) and three output quantities, i.e., the selected natural frequencies of the disk-one-blade assembly (responses), which are used in the identification procedure.

6.4. Identification Framework

The objective of this section is to identify the contact pattern of an unknown blade–root joint based on two sets of input parameters: (i) the blade mistuning parameters, expressed as perturbations of the first three blade modes, and (ii) the natural frequencies of the disk–one-blade assembly corresponding to the 5th, 6th, and 8th modes. The output of the identification procedure is a pair of labels representing the contact patterns on the left and right sides of the joint, each ranging from 1 to 10.

A fundamental limitation of the proposed approach is that the predicted contact patterns are restricted to those contained in the dataset, i.e., one among the 100 possible combinations. The identification is therefore based on selecting the pattern that is dynamically closest to the unknown configuration, in terms of the resulting natural frequencies.

The dataset can be interpreted as a collection of subsets corresponding to different combinations of blade mistuning parameters. Specifically, each triplet of blade mistuning values defines a subset containing 100 possible contact configurations. The structure of the dataset is schematically illustrated in Figure 17. For each combination of blade mistuning parameters $(\delta^1, \delta^2, \delta^3)$, a subset of contact configurations is defined. Each subset consists of all possible combinations of contact patterns on the left and right sides of the blade–disk interface, resulting in a 10×10 grid of 100 configurations. The full dataset is obtained by stacking these subsets along the blade mistuning space. Each layer in Figure 17 therefore corresponds to a specific triplet of blade mistuning parameters, while the in-plane grid represents the contact mistuning space.

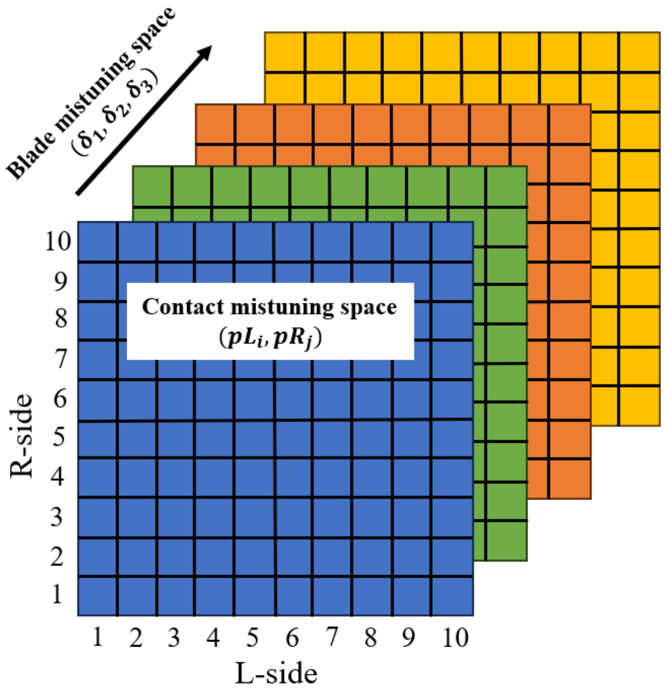

Figure 17. Schematic of the dataset structure: each layer corresponds to a blade mistuning triplet $(\delta^1, \delta^2, \delta^3)$, while the grid represents the contact patterns (pL, pR).

The identification procedure is carried out in two sequential steps, as schematically illustrated in Figure 18. First, the closest triplet of blade mistuning parameters is identified within the dataset using a k-NN search in the blade mistuning space. This step determines the corresponding subset of the dataset, which contains 100 possible contact configurations associated with the selected mistuning parameters. In the second step, the identification is performed within this reduced subset by evaluating the distance between the natural frequencies of the unknown assembly and those stored in the dataset. A k-NN search is then conducted in the frequency space to determine the closest match. The contact configuration associated with this match provides the pair of contact pattern labels (pL, pR). To improve the robustness of the identification in step-2, a weighted distance metric is adopted (Equation (33)). The weights are introduced to account for the different sensitivity of the considered modes to contact variations. In fact, not all modes exhibit the same level of sensitivity, and assigning equal importance to all of them may lead to suboptimal identification performance.

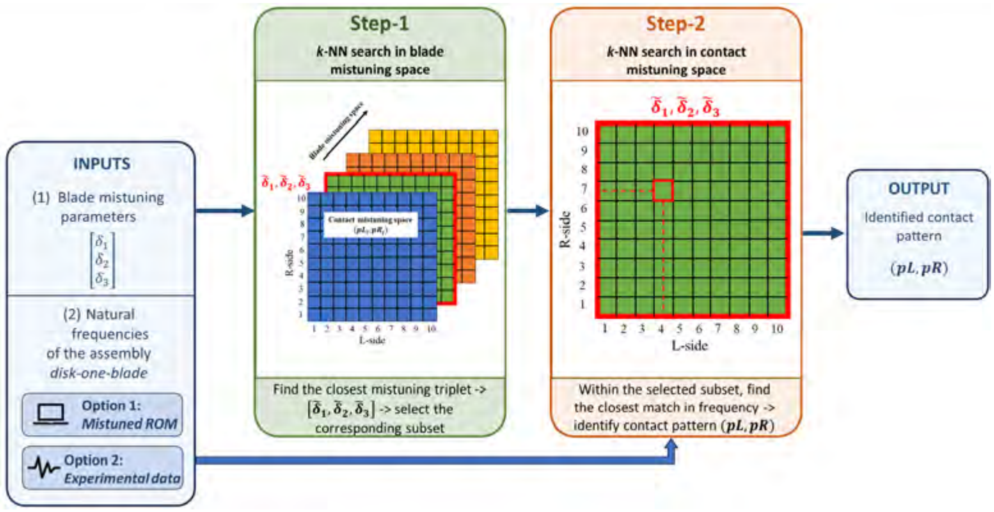

Figure 18. Two-step identification procedure: blade mistuning matching to select a subset, followed by frequency-based search to identify the contact pattern (p_L, p_R).

As discussed in Section 6.2, the selected modes exhibit different levels of variability in their natural frequencies across the considered contact configurations (Figure 15). To ensure that all modal features contribute equally to the Euclidean distance calculation, the natural frequencies are normalized by subtracting their mean value and dividing by the corresponding standard deviation. This normalization places all features on a comparable scale, preventing modes with larger numerical variability from dominating the distance metric. The normalized feature corresponding to the i-th mode is therefore computed as

$$\hat{f}_i = \frac{f_i - \mu_i}{\sigma_i}, \tag{39}$$

where f_i, μ_i, and σ_i denote the natural frequency, the mean value, and the standard deviation of the i-th mode, respectively.

The natural frequencies used as an input to the identification framework are obtained from two different sources:

- *Numerical input:* The natural frequencies are computed using the mistuned ROM of the disk–one-blade assembly, where blade mistuning is introduced using all experimentally identified modes (Table 2), and the contact topology corresponds to experimentally measured patterns (Figure 2). This model serves as an offline digital twin of the physical system, as it incorporates experimentally identified mistuning and contact information into the numerical framework. This case is used as a preliminary validation step to assess the identification framework itself, by ensuring that both the input data and the dataset are generated from the same numerical model. In this way, the correctness of the identification procedure can be verified independently of model discrepancies.
- *Experimental input:* The natural frequencies are obtained from experimental measurements, assuming that the contact pattern is unknown. This represents the actual

application of the identification framework, where the goal is to infer the contact configuration directly from measured data.

7. Results

This section presents the results obtained for both types of inputs: numerical (offline digital twin) and experimental. For both cases, the first k-NN step is identical, as the blade mistuning parameters are uniquely defined and shared between the mistuned ROM and the physical system. Differences may arise in the second k-NN step, since the natural frequencies of the disk–one-blade assembly can slightly differ due to modeling discrepancies between the numerical and experimental systems (Figure 12). In the ideal case of a perfectly representative numerical model, these two inputs would coincide.

Considering the blade mistuning parameters reported in Table 2, the first k-NN step identifies the closest triplet within the discretized dataset, where the mistuning parameters are sampled with a step size of 0.5% (Section 6.3). Since the discretization spans the full range of experimentally observed mistuning values, the closest representation is always available within the dataset.

To assess the accuracy of this step, a normalized error metric is introduced, defined as:

$$\epsilon_i = \frac{\delta_i^{\text{pred}} - \delta_i^{\text{exp}}}{\Delta\delta} \times 100\%, \tag{40}$$

where δ_i^{pred} and δ_i^{exp} denote the predicted and experimental mistuning values of the i-th mode, respectively, and $\Delta\delta = 0.5\%$ is the discretization step. This metric quantifies the relative deviation with respect to the grid resolution of the dataset.

Values of $|\epsilon_i| \leq 50\%$ indicate that the identified mistuning parameters correspond to the closest discretized neighbor, i.e., the correct subset has been selected. Figure 19 shows the evaluation results for the assembly with all blades and the first three modes. As can be observed, all the values of $|\epsilon_i|$ lie within the $\pm 50\%$ interval, confirming that the first k-NN step successfully identifies the closest mistuning triplet.

For the second k-NN step, the validation of the identified contact patterns is carried out through two complementary approaches, as illustrated in Figure 20: geometric validation and dynamic validation:

- **Geometric validation:** This step evaluates the agreement between the predicted and actual contact patterns in terms of their geometric characteristics. While the proposed framework is driven exclusively by dynamic equivalence and does not explicitly enforce geometric consistency, evaluating the resulting contact patterns in terms of their geometric characteristics provides additional insight into the quality of the identification. Two metrics are considered:
  - *Contact area fraction:* This metric quantifies the proportion of the interface in contact and is defined as
  $$A_c = \frac{N_{\text{cont}}}{N_{\text{total}}} \times 100\%, \tag{41}$$
  where N_{cont} is the number of nodes in contact and N_{total} is the total number of interface nodes.
  - *Contact centroid:* This metric captures the spatial distribution of the contact region and is defined as the geometric center of the contacting nodes:
  $$\bar{x} = \frac{1}{N_{\text{cont}}} \sum_{i \in \mathcal{C}} x_i, \qquad \bar{y} = \frac{1}{N_{\text{cont}}} \sum_{i \in \mathcal{C}} y_i, \tag{42}$$

where (x_i, y_i) are the coordinates of the contacting nodes and $\mathcal{C}$ denotes the set of nodes in contact.

- **Dynamic validation:** This step assesses the consistency between predicted and actual contact patterns in terms of their influence on the structural dynamics. The comparison is performed at two levels:
  - *Disk–one-blade assembly:* The natural frequencies and mode shapes are compared between the predicted and reference configurations.
  - *Full-bladed disk assembly:* The validation is extended to the complete system, where natural frequencies and mode shapes are analyzed to ensure that the identified contact pattern reproduces the global dynamic behavior.

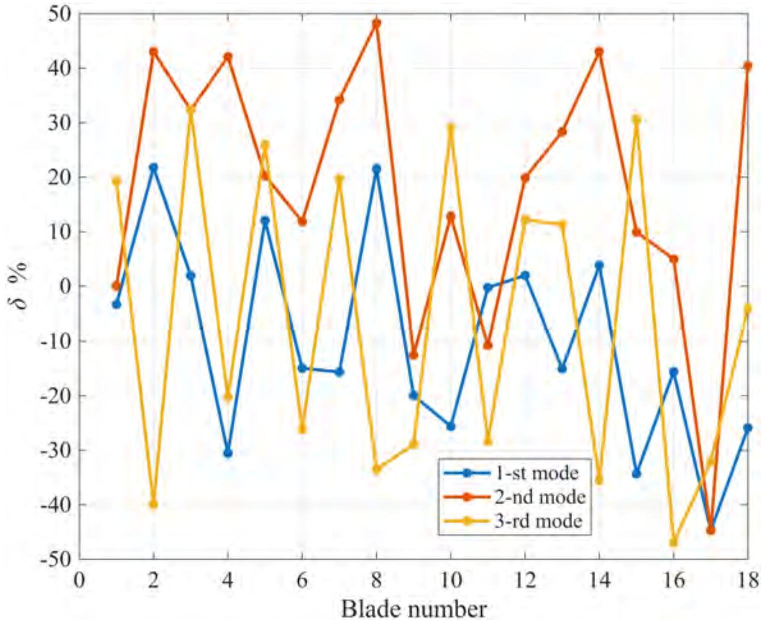

Figure 19. Normalized error of blade mistuning identification for the first three modes.

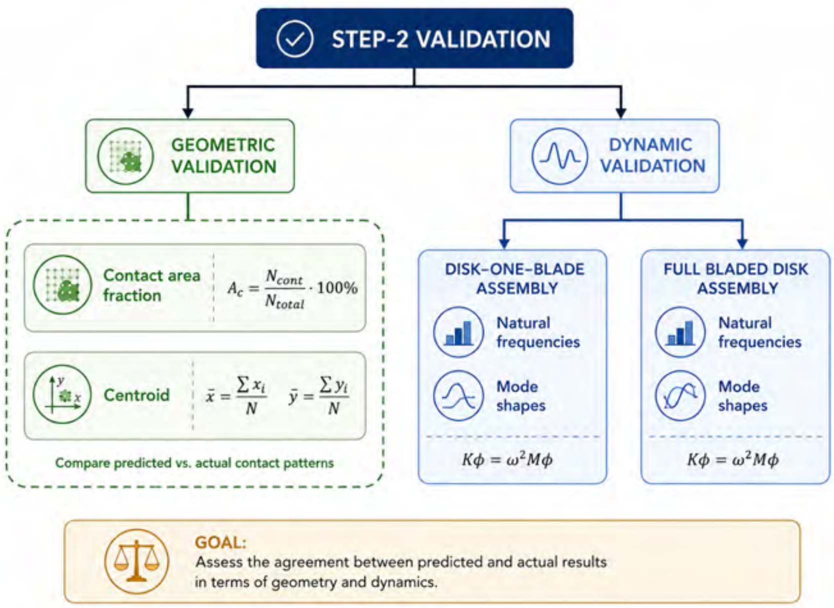

Figure 20. Step-2 validation framework. The identified contact patterns are assessed through geometric validation (contact area fraction and centroid) and dynamic validation at both disk–one-blade and full-bladed disk assembly levels.

7.1. Results Evaluation from the Numerical Input

The geometric validation of the identification framework is first assessed using the numerical input obtained from the offline digital twin. The predicted contact patterns are reported in Table 6.

Table 6. Identified contact patterns from numerical input (offline digital twin).

Joint Index	Left Side	Right Side
1	SP-7	SP-8
2	SP-6	SP-9
3	SP-8	SP-6
4	SP-1	SP-7
5	SP-6	SP-9
6	SP-7	SP-4
7	SP-4	SP-4
8	SP-4	SP-2
9	SP-10	SP-8
10	SP-1	SP-8
11	SP-1	SP-3
12	SP-5	SP-8
13	SP-2	SP-7
14	SP-7	SP-10
15	SP-3	SP-4
16	SP-1	SP-7
17	SP-2	SP-7
18	SP-3	SP-8

The comparison in terms of contact area fraction between the predicted and actual patterns is illustrated in Figure 21. As can be observed, the predicted values generally follow the trend of the actual ones, with moderate deviations. This indicates that, although the identification is not explicitly driven by geometric criteria, the predicted patterns capture a reasonable approximation of the contact extent.

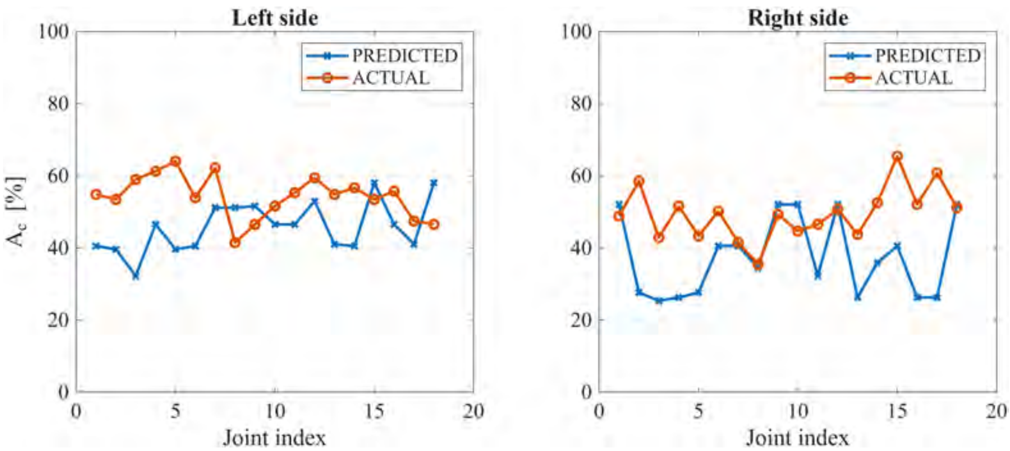

Figure 21. Comparison of contact area fraction between predicted and actual patterns for the left and right sides across all blade–root joints, obtained using numerical input.

Concerning the spatial distribution of the contact, the centroid-based comparison is reported in Figure 22, where representative cases corresponding to the best and worst predictions are shown. In the best case, for the 1st joint, the predicted centroid is in close agreement with the actual one, indicating a good spatial reconstruction of the contact region. In contrast, the worst prediction is observed for the 5th joint, where a deviation between the predicted and actual centroids can be noted. However, the two centroids remain relatively close, indicating that the spatial localization of the contact region is still reasonably captured. This result is consistent with the fact that the identification procedure is driven solely by dynamic equivalence and does not explicitly enforce geometric matching.

(**a**) Best prediction case

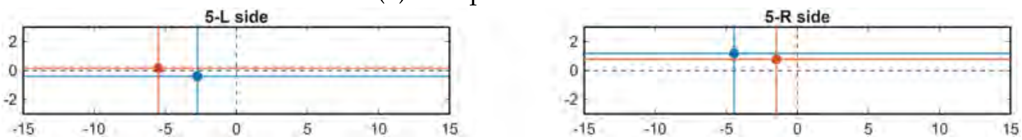

(**b**) Worst prediction case

Figure 22. Centroid comparison between predicted and actual contact patterns, obtained using numerical input. The red marker denotes the centroid of the actual pattern, while the blue marker denotes the centroid of the predicted pattern.

The dynamic validation at the disk–one-blade assembly level is illustrated in Figure 23. The figure reports, for the 5th, 6th, and 8th modes, the comparison between predicted and actual natural frequencies across all blade–root joints (top row), the corresponding relative differences (middle row), and the MAC values between the associated mode shapes (bottom row).

It is important to note that this validation is not straightforward, as the numerical model used to construct the dataset and to generate the input for the identification differ in two key aspects. First, blade mistuning in the dataset is introduced by perturbing only the first three blade modes, whereas the mistuned ROM used to generate the input frequencies incorporates perturbations in all experimentally identified blade modes. Second, contact mistuning in the dataset is limited to the set of synthetically generated patterns, while the input frequencies are obtained using exclusively experimentally measured contact patterns.

Despite these differences, the results demonstrate a very good agreement between predicted and actual natural frequencies for all three modes, with deviations remaining small across all joints. The relative differences are generally close to zero, with only a few localized peaks. Furthermore, the MAC values are consistently close to unity, confirming an excellent correlation between the predicted and actual mode shapes.

The dynamic validation is finally extended to the full-bladed disk assembly. After identifying the contact patterns at all blade–root joints, the predicted configuration is assembled and its modal parameters are compared against that of the reference system with experimentally measured contact patterns. This step is crucial, as it provides a global assessment of the identification framework based on dynamic equivalence.

The results are reported in Figure 24. The validation is carried out on the set of mistuned modes associated with the first three modal families of the tuned assembly, which represent the target modes considered in this study (see Section 6.3). The middle panel presents the corresponding relative differences, while the bottom panel reports the diagonal values of the MAC matrix, allowing for a direct assessment of the correlation between predicted and actual mode shapes. Only the diagonal terms are shown to enhance the readability of the numerical values. As can be observed, the predicted natural frequencies closely match the reference ones across the entire spectrum, with only minor deviations. The relative differences remain small, indicating a high level of accuracy in capturing the eigenvalues of the system. In addition, the MAC values are consistently high for the majority of the modes, confirming a strong agreement between the predicted and actual mode shapes.

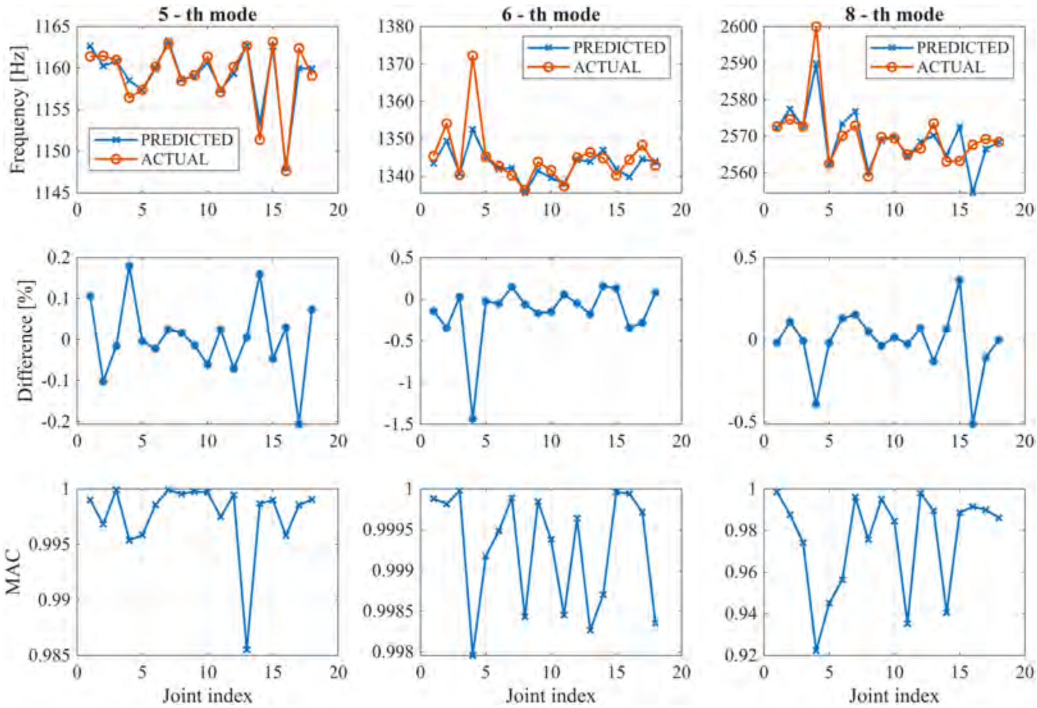

Figure 23. Comparison of predicted and actual modal parameters for the disk–one-blade assembly using input from the offline digital twin: natural frequencies, relative differences, and MAC values for the 5th, 6th, and 8th modes.

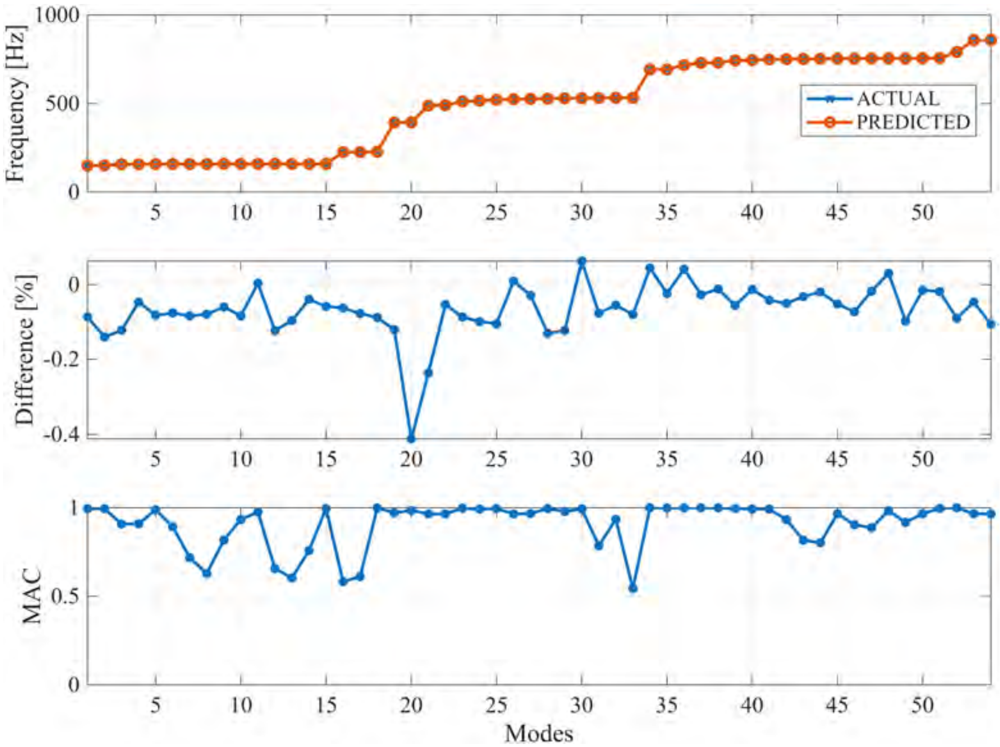

Figure 24. Comparison of predicted and actual dynamics of the full-bladed disk assembly using input from the offline digital twin: natural frequencies, relative differences, and diagonal MAC values.

7.2. Results Evaluation from the Experimental Input

The predicted contact patterns obtained using the experimental input are reported in Table 7. In this stage, the identification framework is driven by experimental data, where the natural frequencies of the disk–one-blade assembly are extracted from hammer test measurements performed on the real physical structure. These frequencies are then used as input to the identification algorithm.

The geometric validation is first assessed in terms of contact area fraction. The comparison between predicted and actual area fractions for both left and right sides of each blade–root joint is reported in Figure 25. Overall, the predicted values follow the same trend as the experimental ones across the majority of the joints, indicating that the identification framework captures the global distribution of contact.

The geometric validation is further assessed in terms of the centroid of the contact pattern. For clarity, only representative cases corresponding to the best and worst agreement are reported in Figure 26. The top row shows the case of joint 15, which exhibits the best agreement between predicted and actual centroids for both left and right sides. In this case, the predicted and measured centroids are nearly coincident, indicating an accurate reconstruction of the spatial distribution of the contact area. The bottom row reports the case of joint 8, corresponding to the largest deviation. Although a shift between predicted and actual centroids can be observed, the discrepancy remains limited and the predicted location still lies within the same region of the contact interface.

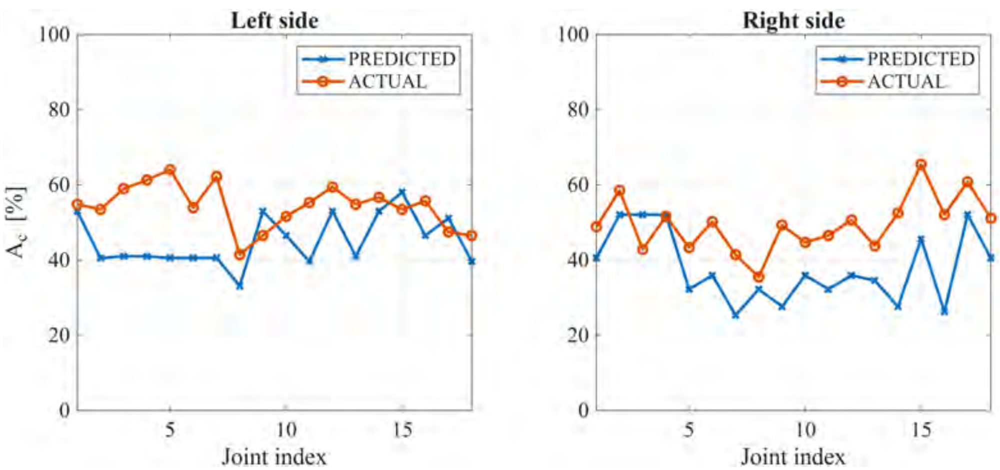

Figure 25. Comparison of predicted and actual contact area fraction A_c for the left and right sides of all blade–root joints, obtained using experimental input.

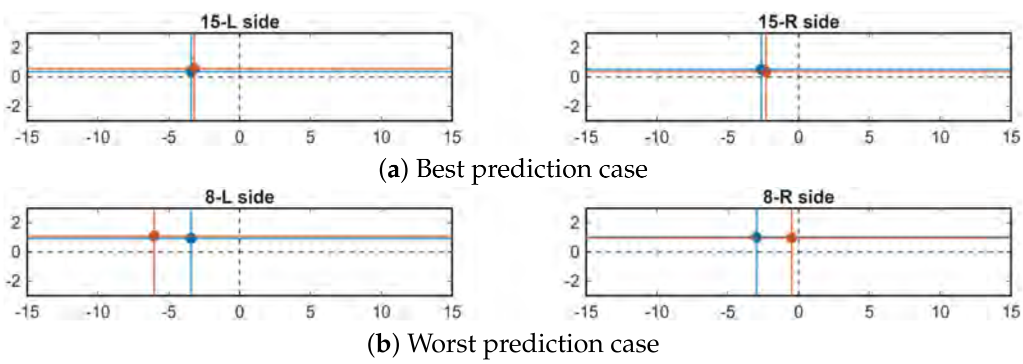

Figure 26. Centroid comparison between predicted and actual contact patterns for the experimental input. The red marker denotes the centroid of the actual pattern, while the blue marker denotes the centroid of the predicted pattern.

Table 7. Predicted contact patterns from experimental input.

Blade–Root Joint Index	Left Side	Right Side
1	SP-5	SP-4
2	SP-7	SP-8
3	SP-2	SP-8
4	SP-2	SP-8
5	SP-7	SP-3
6	SP-7	SP-10
7	SP-7	SP-6
8	SP-9	SP-3
9	SP-5	SP-9
10	SP-1	SP-10
11	SP-6	SP-3
12	SP-5	SP-10
13	SP-2	SP-2
14	SP-5	SP-9
15	SP-3	SP-1
16	SP-1	SP-7
17	SP-4	SP-8
18	SP-6	SP-4

The dynamic validation at the disk–one-blade assembly level using experimental input is reported in Figure 27. The figure presents, for the 5th, 6th, and 8th modes, the comparison between predicted and experimentally identified natural frequencies (top row), the corresponding relative differences (middle row), and the MAC values between predicted and experimental mode shapes (bottom row). Overall, a good agreement is observed between predicted and experimental natural frequencies, with deviations remaining limited across all joints. The relative differences are generally small. The MAC values are also high for the majority of the modes, indicating a strong correlation between predicted and measured mode shapes. A noticeable reduction in MAC values is observed for the 8th mode. This behavior is not attributed to inaccuracies in the identification process, but rather to experimental limitations. In particular, this mode exhibits low mobility in the direction of the vibration measurement, resulting in a reduced signal-to-noise ratio. Consequently, the experimentally identified mode shapes are more affected by measurement noise, which leads to lower MAC values.

The final validation is performed at the level of the full-bladed disk assembly using experimental input. The predicted configuration, obtained from the identification of all blade–root joints, is assembled and its dynamic response is compared with the experimentally measured one. The results are reported in Figure 28, which shows the comparison between predicted and experimental natural frequencies (top), the corresponding relative differences (middle), and the diagonal values of the MAC matrix (bottom). A very good agreement is observed between predicted and experimental natural frequencies over the entire spectrum. The relative differences remain small for the majority of the modes, with only a few localized deviations. The MAC values are generally high, confirming a strong correlation between predicted and experimentally identified mode shapes of the full mistuned assembly. Some localized reductions in MAC values can be observed for a limited number of modes. Similarly to the disk–one-blade case, these discrepancies are mainly attributed to experimental limitations, such as reduced signal-to-noise ratio, rather than to inaccuracies in the identification procedure. Overall, these results demonstrate that the proposed identification framework, despite being based on synthetic contact representations, is capable of reconstructing the dynamics of the full mistuned bladed disk with a high level of accuracy.

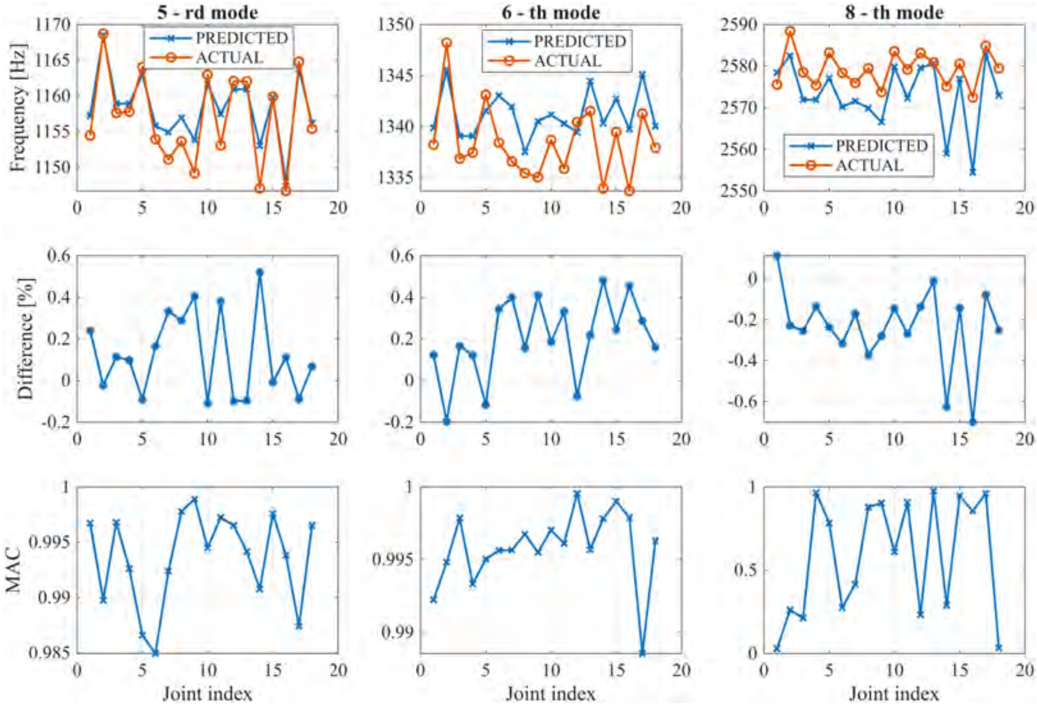

Figure 27. Comparison of predicted and actual dynamics for the disk–one-blade assembly using experimental input: natural frequencies, relative differences, and MAC values for the 5th, 6th, and 8th modes.

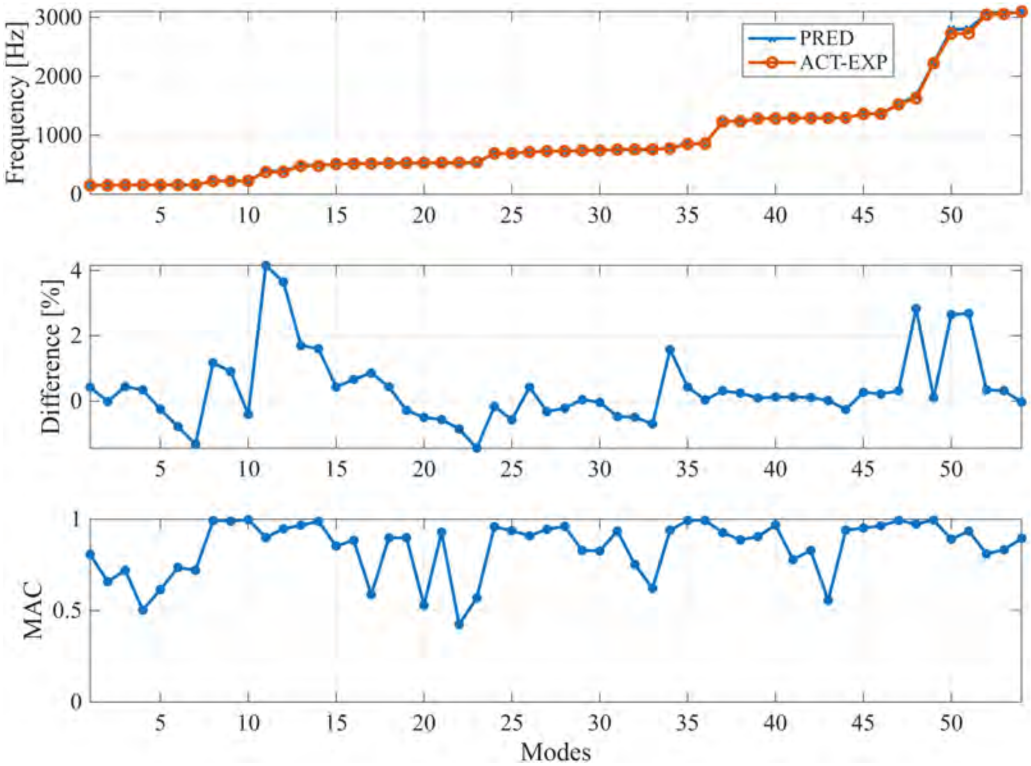

Figure 28. Comparison of predicted and actual dynamics of the full-bladed disk assembly using experimental input: natural frequencies, relative differences, and diagonal MAC values.

8. Discussion

The results presented in the previous sections provide a comprehensive assessment of the proposed identification framework from both geometric and dynamic perspectives

From a geometric standpoint, both the contact area fraction and the centroid of the predicted patterns show a good agreement with the experimentally observed ones for both types of inputs. This behavior is partly expected due to the repetitive nature of the contact patterns on either side of the blade–root joint, which exhibit similar spatial characteristics. Nevertheless, it is noteworthy that, for several joints (see Figures 21, 22, 25, and 26), the predicted and actual values of area fraction and centroid are nearly identical. This result is particularly interesting, as the identification procedure does not explicitly target geometric matching, but relies solely on dynamic equivalence. The ability to recover meaningful geometric descriptors therefore highlights the representativeness and richness of the dataset, within which sufficiently similar patterns can be identified.

At the disk–one-blade level, the dynamic validation shows an excellent agreement between predicted and actual natural frequencies for both numerical and experimental inputs, with discrepancies remaining well below 1%. This result is consistent with the formulation of the identification procedure, which directly relies on natural frequencies as input features. More importantly, the high level of agreement indicates that the dataset is sufficiently rich and descriptive, covering a sufficiently broad range of frequency values to allow for accurate matching even when the exact contact pattern is not explicitly included in the dataset. In addition, the MAC values confirm a strong correlation between predicted and actual mode shapes, despite the fact that mode shapes are not explicitly used in the identification process. This observation further supports the conclusion that the identified patterns are dynamically equivalent not only in terms of eigenvalues, but also in terms of eigenvectors.

The most critical validation is obtained at the level of the full-bladed disk assembly. While the agreement observed at the disk–one-blade level is partly expected, as the identification is performed at that scale, it does not necessarily guarantee dynamic equivalence at the full system level. The results demonstrate that the predicted contact patterns lead to modal parameters that closely matches the one obtained using the actual patterns, both in terms of natural frequencies and mode shapes (see Figure 24). This confirms that the identification based on disk–one-blade dynamics is sufficient to capture the effect of contact mistuning at the scale of the full assembly. In particular, the high MAC values indicate that key phenomena associated with mistuning, such as mode localization, is also correctly reproduced.

A slightly reduced accuracy is observed for the experimental input compared to the numerical input. This discrepancy may be attributed either to limitations of the identification framework or to uncertainties associated with the experimental–numerical comparison. The latter may arise from the inability of the numerical model to fully reproduce the behavior of the physical system and/or the limited accuracy of the experimentally identified modal parameters. In particular, some mode shapes may be significantly affected by measurement noise when the structural mobility in the measurement direction is low, leading to less reliable experimental mode shape identification. To better understand the origin of these discrepancies, it is useful to refer to the validation results presented in Section 5, where the mistuned ROM with experimentally measured blade and contact mistuning was compared against experimental measurements (Figure 13). The presence of similar discrepancies, e.g., peaks in frequency errors and reduced MAC values for specific modes such as 11, 12, 34, 48, 51, and 52 (see Figures 13 and 28), in both comparisons, namely between the experimental data and the mistuned ROM with actual experimentally measured patterns, and between the experimental data and the mistuned ROM with predicted patterns, indicates that these deviations originate from uncertainties in the experimental and numerical representations of the system rather than from the identification procedure.

https://doi.org/10.3390/app16157648

To quantify these observations, the mean absolute error in natural frequencies and the mean MAC values are evaluated over all considered modes for the three validation scenarios defined below:

- **Case A:** Mistuned ROM with predicted contact patterns, where the identification input is generated from the offline digital twin with experimentally measured contact patterns (Section 7.1), compared against the mistuned ROM with actual experimentally measured contact patterns.
- **Case B:** Mistuned ROM with predicted contact patterns, where the identification input is obtained from experimental measurements (Section 7.2), compared against the experimental data.
- **Case C:** Mistuned ROM with actual experimentally measured contact patterns compared against the experimental data (Section 5).

The results are summarized in Table 8. As can be observed, Case A exhibits the best overall agreement, with a mean absolute frequency error of only 0.07% and a mean MAC value equal to 0.91. Since both the dataset and the identification input originate from the same numerical framework, these results primarily reflect the intrinsic accuracy of the identification procedure itself. The degradation in performance for the experimental input closely follows the intrinsic accuracy of the ROM, confirming that the identification framework itself remains robust. Overall, the results obtained with the experimental input demonstrate a good level of agreement, with the mean absolute frequency error remaining below 1% and the mean MAC values staying consistently high. These observations indicate that the proposed framework is capable of accurately reproducing the dynamic behavior of the mistuned assembly when driven exclusively by experimental measurements. Therefore, the methodology represents a promising approach for practical applications, where experimental input is the only available source of information.

Table 8. Summary of dynamic prediction accuracy for the full-bladed disk assembly.

	Case A	Case B	Case C
Mean absolute error in f_{nat} [%]	0.07	0.73	0.46
Mean MAC	0.91	0.85	0.82

The proposed approach, however, presents several limitations:

- **Non-generative identification framework:** The proposed methodology is not generative, as the identification is restricted to the set of contact patterns contained in the dataset. Consequently, the predicted pattern is always selected among pre-defined synthetic configurations. Developing a fully generative identification framework would require describing the contact topology through a very large number of parameters. In the present case, the contact interface is discretized by a 7×31 grid, resulting in 217 interface nodes. Since each node can assume two possible states, namely contact or no-contact, the total number of possible configurations becomes extremely large, making a direct generative approach computationally impractical. A possible alternative would consist in describing the contact patterns using simplified parameterized geometries, such as rectangular contact regions. This would drastically reduce the number of parameters required to define the contact topology. However, such simplifications would also reduce the representativeness of the patterns with respect to experimentally observed contact families, leading to contact topologies that no longer resemble realistic experimental patterns.
- **Dependence on dataset richness:** The identification accuracy strongly depends on the richness and descriptiveness of the dataset. Since the framework is based on dynamic

equivalence, the dataset must span a sufficiently broad range of natural frequency variations to ensure that dynamically equivalent patterns can be identified. If the dataset does not adequately cover the possible range of values, the closest identified configuration may not correctly represent the actual contact condition.
- **Dependence on numerical model accuracy:** The methodology relies on the accuracy of the numerical model used to construct the dataset. While the dataset is generated numerically, the identification input is obtained experimentally. Any discrepancy between the numerical model and the actual physical system therefore introduces a bias between the dataset and the measured data, which may affect the accuracy of the k-NN matching and, consequently, the identified contact patterns.

Despite these limitations, the proposed framework offers promising perspectives for practical applications. In particular, it enables the construction of high-fidelity numerical models that account for realistic contact mistuning without requiring exhaustive experimental measurement of each blade–root joint. By relying on easily measurable dynamic quantities, such as natural frequencies, the approach significantly reduces the experimental effort while maintaining a high level of accuracy in the prediction of the assembly dynamics.

9. Conclusions

This work proposed a data-driven framework for the identification of contact mistuning in bladed disks using limited experimental data. The methodology combines a ROM strategy with PCA-based generation of synthetic contact patterns and a k-NN identification procedure based on natural frequencies of a disk–one-blade assembly. The identified contact patterns were subsequently validated both geometrically and dynamically, at the scale of the individual joint and at the scale of the full mistuned bladed disk assembly.

The results demonstrated that the proposed PCA framework is capable of generating synthetic contact patterns that preserve the main spatial characteristics observed in the experimentally measured pressure-film imprints. Despite the identification being entirely based on dynamic equivalence rather than geometric matching, the predicted patterns showed good agreement with the actual experimental patterns in terms of both contact area fraction and centroid position. In several cases, the predicted and measured patterns exhibited almost identical geometric descriptors. The dynamic validation of the disk–one-blade assembly showed excellent agreement between the assemblies constructed using the predicted and actual contact patterns. For both numerical and experimental inputs, the discrepancies in natural frequencies generally remained below 1%, while the corresponding mode shapes exhibited high MAC values. The most important validation concerned the full mistuned bladed disk assembly. The comparison between the full-bladed disk models constructed using predicted and experimentally measured contact patterns demonstrated very good agreement in both natural frequencies and mode shapes.

For the case involving experimental input, larger discrepancies were observed for a limited number of modes. However, comparison with the validation of the mistuned ROM against the experimental measurements showed that these discrepancies originate primarily from the uncertainties in the experimental and numerical representations of the system rather than from the identification framework itself. This observation was further confirmed by the comparison of the mean absolute frequency errors and mean MAC values for the different validation scenarios. Even in the experimental case, the average frequency error remained below 1%, while the MAC values stayed generally high.

The study also highlighted several limitations of the proposed framework. First, the identification is not generative, since the predicted pattern is selected among pre-defined patterns contained in the dataset. Second, the quality of the identification strongly depends on the richness of the dataset and its ability to adequately span the admissible range of natural frequencies associated with contact variability. Third, the methodology relies on the accuracy of the numerical model used to represent the physical system, since any discrepancy between the numerical and experimental dynamics introduces a bias in the identification process.

Despite these limitations, the proposed framework represents a practical and computationally efficient strategy for the identification of contact mistuning in bladed disks. By relying only on experimentally measurable modal quantities, such as natural frequencies, the methodology significantly reduces the experimental effort required to characterize the blade–disk joints. The proposed approach therefore provides a promising basis for the development of experimentally informed digital twins of mistuned bladed disks and for future studies on the influence of contact variability on system dynamics. Future work will focus on extending the proposed methodology to nonlinear contact conditions by incorporating friction-induced interface effects into the reduced-order model and validating the resulting framework through dedicated experimental investigations.

Author Contributions: Conceptualization, U.U., C.M.F. and G.B.; methodology, U.U., C.M.F. and G.B.; software, U.U.; validation, U.U., C.M.F. and G.B.; formal analysis, U.U.; investigation, U.U.; resources, C.M.F. and G.B.; data curation, U.U.; writing—original draft preparation, U.U.; writing—review and editing, C.M.F. and G.B.; visualization, U.U.; supervision, C.M.F. and G.B.; project administration, C.M.F. and G.B. All authors have read and agreed to the published version of the manuscript.

Funding: This research received no external funding.

Institutional Review Board Statement: Not applicable.

Informed Consent Statement: Not applicable.

Data Availability Statement: The datasets generated and analyzed during the current study are available from the corresponding author upon reasonable request.

Conflicts of Interest: The authors declare no conflicts of interest.

Abbreviations

The following abbreviations are used in this manuscript:

PCA	Principal Component Analysis
k-NN	k-Nearest Neighbors
FEM	Finite Element Model
ROM	Reduced-Order Model
DOF	Degrees of Freedom
CB-CMS	Craig–Bampton Component Mode Synthesis
EMA	Experimental Modal Analysis
LDV	Laser Doppler Vibrometry
LSRF	Least Squares Rational Fraction
FRF	Frequency Response Function
CAD	Computer-Aided Design
BR	Blade Root
MAC	Modal Assurance Criterion
SP	Synthetic Pattern
SVD	Singular Value Decomposition

References

1. Tobias, S.A.; Arnold, R.N. The influence of dynamical imperfection on the vibration of rotating disks. *Proc. Inst. Mech. Eng.* **1957**, *171*, 669–690. [CrossRef]
2. Wagner, J.T. Coupling of turbomachine blade vibrations through the rotor. *J. Eng. Power* **1967**, *89*, 502–512. [CrossRef]
3. Whitehead, D.S. Effect of mistuning on the vibration of turbo-machine blades induced by wakes. *J. Mech. Eng. Sci.* **1966**, *8*, 15–21. [CrossRef]
4. Kenyon, J.A.; Griffin, J.H. Forced response of turbine engine bladed disks and sensitivity to harmonic mistuning. *J. Eng. Gas Turbines Power* **2002**, *125*, 113–120. [CrossRef]
5. Yang, M.-T.; Griffin, J.H. A reduced-order model of mistuning using a subset of nominal system modes. *J. Eng. Gas Turbines Power* **1999**, *123*, 893–900. [CrossRef]
6. Castanier, M.P.; Óttarsson, G.; Pierre, C. A reduced order modeling technique for mistuned bladed disks. *J. Vib. Acoust.* **1997**, *119*, 439–447. [CrossRef]
7. Petrov, E.P.; Sanliturk, K.Y.; Ewins, D.J. A new method for dynamic analysis of mistuned bladed disks based on the exact relationship between tuned and mistuned systems. *J. Eng. Gas Turbines Power* **2002**, *124*, 586–597. [CrossRef]
8. Petrov, E.P.; Ewins, D.J. Analysis of the worst mistuning patterns in bladed disk assemblies. *J. Turbomach.* **2003**, *125*, 623–631. [CrossRef]
9. Feiner, D.M.; Griffin, J.H. A fundamental model of mistuning for a single family of modes. *J. Turbomach.* **2002**, *124*, 597–605. [CrossRef]
10. Bladh, R.; Castanier, M.P.; Pierre, C. Component-mode-based reduced order modeling techniques for mistuned bladed disks: Part I—Theoretical models. *J. Eng. Gas Turbines Power* **2001**, *123*, 89–99.
11. Bladh, R.; Castanier, M.P.; Pierre, C. Component-mode-based reduced order modeling techniques for mistuned bladed disks: Part II—Application. *J. Eng. Gas Turbines Power* **2001**, *123*, 89–99.
12. Lim, S.H.; Bladh, R.; Castanier, M.P.; Pierre, C. A compact, generalized component mode mistuning representation for modeling bladed disk vibration. In Proceedings of the 44th AIAA/ASME/ASCE/AHS Structures, Structural Dynamics, and Materials Conference, Norfolk, Virginia, 7–10 April 2003; Volume 2, pp. 1359–1380.
13. Krizak, T.; D'Souza, K. A generalized model of mistuning for bladed disks. *J. Sound. Vib.* **2025**, *606*, 119003. [CrossRef]
14. Beck, J.A.; Brown, J.M.; Runyon, B.; Scott-Emuakpor, O.E. Probabilistic study of integrally bladed rotor blends using geometric mistuning models. In *AIAA SciTech Forum*; American Institute of Aeronautics and Astronautics: Reston, VA, USA, 2017.
15. Beck, J.A.; Brown, J.M.; Kaszynski, A.A.; Carper, E.B.; Gillaugh, D.L. Geometric mistuning reduced-order model development utilizing Bayesian surrogate models for component mode calculations. *J. Eng. Gas Turbines Power* **2019**, *141*, 091013. [CrossRef]
16. Beck, J.A.; Brown, J.M.; Slater, J.C.; Cross, C.J. Probabilistic mistuning assessment using nominal and geometry based mistuning methods. *J. Turbomach.* **2013**, *135*, 051004. [CrossRef]
17. Madden, A.; Epureanu, B.I.; Filippi, S. Reduced-order modeling approach for blisks with large mass, stiffness, and geometric mistuning. *AIAA J.* **2012**, *50*, 366–374. [CrossRef]
18. Krizak, T.; Kurstak, E.; D'Souza, K. Damping and stiffness mistuning effects in a bladed disk with varied disk coupling. *J. Eng. Gas Turbines Power* **2024**, *146*, 011018. [CrossRef]
19. Anish, G.; Joshi, S.; Epureanu, B. Reduced order models for blade-to-blade variability in mistuned blisks. *J. Vib. Acoust.* **2012**, *134*. [CrossRef]
20. Saeed, Z.; Firrone, C.M.; Berruti, T.M. Joint Identification through Hybrid Models Improved by Correlations. *J. Sound. Vib.* **2021**, *494*, 115889. [CrossRef]
21. Battiato, G.; Firrone, C.M. Reduced Order Modeling of Large Contact Interfaces to Calculate the Non-Linear Response of Frictionally Damped Structures. *Procedia Struct. Integr.* **2020**, *24*, 837–851. [CrossRef]
22. Battiato, G. Self-Adaptive Macroslip Array for Friction Force Prediction in Contact Interfaces with Non-Conforming Meshes. *Nonlinear Dyn.* **2021**, *106*, 745–764. [CrossRef]
23. Petrov, E.P.; Ewins, D.J. Method for analysis of nonlinear multiharmonic vibrations of mistuned bladed disks with scatter of contact interface characteristics. *J. Turbomach.* **2005**, *127*, 128–138. [CrossRef]
24. Avalos, J.; Mignolet, M.P.; Soize, C. Response of bladed disks with mistuned blade-disk interfaces. In *ASME Turbo Expo 2009: Power for Land, Sea, and Air*; ASME: New York, NY, USA, 2009; pp. 323–332.
25. Krizak, T.; Firrone, C.; Battiato, G.; D'Souza, K. A bladed disk reduction technique that captures variation in blade stiffness and blade root joint contacts. In *ASME Turbo Expo 2024: Turbomachinery Technical Conference and Exposition*; ASME: New York, NY, USA, 2024; p. V10BT27A034.
26. Pinto, V.; Battiato, G.; Firrone, C.M. Reduced order models for bladed disks with contact mistuning at blade root joints. In *ASME Turbo Expo 2023: Turbomachinery Technical Conference and Exposition*; ASME: New York, NY, USA, 2023; Volume 11B, p. V11BT23A006.

27. Battiato, G.; Firrone, C.M.; Berruti, T.M.; Epureanu, B.I. A General Method for Sub-Systems Coupling for the Dynamic Analysis. In *Proceedings of the International Conference on Noise and Vibration Engineering (ISMA 2016)*; Katholieke Universiteit Leuven: Leuven, Belgium, 2016; pp. 3433–3446.
28. Pinto, V.; Battiato, G.; Firrone, C.M. A reduction technique for the calculation of the forced response of bladed disks in the presence of contact mistuning at blade root joints. *J. Eng. Gas Turbines Power* **2022**, *145*, 021013. [CrossRef]
29. Usmanov, U.; Firrone, C.M.; Battiato, G. Prediction of Blade–Disk Contact Mistuning Patterns Using Probabilistic and Machine Learning Methods. In *Proceedings of the ASME Turbo Expo 2026: Turbomachinery Technical Conference and Exposition (GT2026)*; Paper GT2026-177381; American Society of Mechanical Engineers (ASME): Milan, Italy, 2026.
30. Usmanov, U.; Firrone, C.M.; Battiato, G. Data-Driven Prediction of Blade–Disk Contact Mistuning From Modal Characteristics. In *Proceedings of the ASME Turbo Expo 2026: Turbomachinery Technical Conference and Exposition (GT2026)*; Paper GT2026-178679; American Society of Mechanical Engineers (ASME): Milan, Italy, 2026.
31. Craig, R.R.; Bampton, M.C.C. Coupling of substructures for dynamic analyses. *AIAA J.* **1968**, *6*, 1313–1319. [CrossRef] [PubMed]
32. Rubin, S. Improved component-mode representation for structural dynamic analysis. *AIAA J.* **1975**, *13*, 995–1006. [CrossRef]
33. Craig, R.R.; Kurdila, A.J. *Fundamentals of Structural Dynamics*, 2nd ed.; John Wiley & Sons: Hoboken, NJ, USA, 2006.
34. Voormeer, S.N. Dynamic Substructuring Methodologies for Integrated Dynamic Analysis of Wind Turbines. Ph.D. Thesis, Delft University of Technology, Delft, The Netherlands, 2012.
35. Cover, T.; Hart, P. Nearest neighbor pattern classification. *IEEE Trans. Inf. Theory* **1967**, *13*, 21–27. [CrossRef]
36. Verboven, P.; Vanlanduit, S.; Van der Auweraer, H.; Peeters, B. A poly-reference implementation of the least-squares complex frequency-domain estimator. In *Proceedings of IMAC*; Society for Experimental Mechanics: Orlando, FL, USA, 2003.
37. European Committee for Standardization (CEN). *EN 10083-2:2006 Steels for Quenching and Tempering—Part 2: Technical Delivery Conditions for Non-Alloy Steels*; CEN: Brussels, Belgium, 2006.